Crystal-defect engineering of electrode materials for energy storage and conversion.

WANG, J., ZHAO, X., ZOU, G., ZHANG, L., HAN, S., LI, Y., LIU, D., FERNANDEZ, C., LI, L., REN, L. and PENG, Q.

2023

Crystal-defect engineering of electrode materials for energy storage and conversion

Jinming Wang [1], Xue Zhao [1], Guodong Zou [1], Lu Zhang [1], Shumin Han [1], Yueming Li [1], Di Liu [1], Carlos Fernandez [2], Lanjie Li [3], Liqun Ren [4] and Qiuming Peng*[1]

[1] *CNEC, State Key Laboratory of Metastable Materials Science and Technology, School of Materials Science and Engineering, Yanshan University, Qinhuangdao 066004, China.*

[2] *School of Pharmacy and Life Sciences, Robert Gordon University, AB107GJ Aberdeen, UK.*

[3] *Chengde Iron and Steel Group Co., Ltd, HBIS Group Co., Ltd, Chengde, Hebei 067102, China.*

[4] *Laboratory of Spinal Cord Injury and Rehabilitation, Chengde Medical University, Chengde 067000, China.*

Corresponding author E-mail: pengqiuming@ysu.edu.cn

Abstract

Crystal-defect engineering (CDE) in electrode materials is an emerging research area for tailoring properties, which opens up unprecedented possibilities not only in battery and catalysis, but also in controlling physical, chemical, and electronic properties. In the past few years, numerous types of research have been performed to alter the surface/interface electronic structure of electrode materials or to optimize the physical and chemical properties of electrode materials, which improves their electrochemical performance. However, it is still challenging to describe the effects of the inherent or intentionally created defects of various types on energy storage and energy conversion systems, dependent on the perspective of crystal structural defects. In this review, the definition, classification, characterization, and model simulation of crystal defects are firstly described. Subsequently, the manufacturing methods of crystal defects and the application of different kinds of crystal defects in the fields of batteries and catalysis are emphasized. Finally, the potential challenges and opportunities of defective electrode materials in relation to controllable preparation, in-situ characterization, and commercial applications are discussed, providing a perspective for future development.

Keywords: crystal defects; electrode materials; energy storage; energy conversion; catalyst

1. Introduction

The reserve limitations of fossil fuels, such as coal, petroleum, and natural gas, and their adverse impact on environmental protection become two unavoidable factors in developing an alternative, sustainable, and clean energy technology [1-3].Actually, solar, wind, and geothermal resources are becoming the fastest-growing sources of power generation in the world. However, owing to some inherent characteristics of intermittent and geographical dispersion, energy storage and conversion systems are considered extremely significant means for their efficient utilization [4]. In a sustainable system, the electricity created from these renewable sources can either be stored directly in rechargeable batteries as a power source or turned into clean fuel through electrolytic cells and then converted into electricity by fuel cells [5]. These devices work using various mechanisms, they apply a similar configuration, in which two independent electrodes are ionically coupled *via* an electrolyte [6]. Since all reactions of the above devices take place on the electrodes, the development of novel high-efficiency electrode materials is of great practical significance for improving the efficiency of electrochemical energy storage and conversion systems.

In the past decade, owing to the complexity and diversity of structure, increasingly advanced characterization techniques have been developed to reveal the influence of internal structure within electrode materials on electrochemical properties [7]. Researchers have altered the composition, size, morphology, dimension, porosity, crystal structure, and electrical conductivity of the electrode through rational design strategies, resulting in a good structure-performance relationship [8-10]. On the one hand, morphological control provides a large specific surface area and porous/hollow structure to facilitate ion adsorption/intercalation and relieve structural strain to accommodate serious volume changes. On the other hand, material composition strategies can improve electrical conductivity and electrochemical reactivity, such as combining transition metal oxides with conductive materials [11-13]. Although the above two methods are simple and efficient, they do not

change the modification of the atomic/electronic structure of matrix materials, which is the "extrinsic" method. As a result, the enhancement of electrode performance is minimal. More recently, a novel "intrinsic" strategy based on the intentional introduction of defects into the lattice structure of matrix materials has received increasing attention [14, 15]. Compared with the "extrinsic" strategies, the newly emerging CDE-based on "intrinsic" strategies can mainly manipulate the local atomic structure/coordination environment of electrode material in a controllable manner, enabling an efficient "intrinsic" strategy to tune the electronic and structural properties of electrode materials [16, 17]. Therefore, excellent electrochemical performance can be achieved by lowering the diffusion barrier, providing additional intercalation sites, and improving electrode kinetics. Basically, there are various types of intrinsic crystal defects in electrode materials, such as point, line, and plane defects, which can be obtained by different processing methods (**Fig. 1**) [18-23]. Moreover, due to the complex diversity of defect structures, various types concentrations, and distributions of crystal defects in electrode materials often have variable effects on reactivity [24, 25]. Therefore, as the smallest unit that affects the performance of electrode materials, crystal defects guide the construction of electrode materials and the development of the entire energy storage and conversion system [26-28]. However, few articles have discussed the relationship between crystal defect types and electrochemical performance. Moreover, it remains challenging to describe the effects of various types of inherent or intentionally generated defects on energy storage and conversion systems from the perspective of crystal defects. Therefore, the purpose of this review is mainly to clarify the types of defects and the contribution of various types of defects in electrochemical energy storage and conversion systems, and how to guide the construction of electrode materials from the perspective of defects. This will open up new directions for crystal defect engineering and clarify the mechanism for the performance enhancement of defect-rich electrode materials in electrochemical storage and conversion systems.

Herein, we primarily discuss the conception of different defects, analyze the principle of inducing defects of each method, and elaborate on two aspects of benefits and drawbacks. Subsequently, we concentrate on the uniqueness of each internal crystal defect, such as the controllable introduction of crystal defects and the performance-enhancing mechanism of defect electrodes, which are extremely helpful in broadening our understanding of electrochemical energy storage and conversion processes. Finally, we summarize the challenges and opportunities of CDE of electrode materials for energy storage and conversion applications.

2. Crystal defect engineering

2.1. Definition of crystal defects

A certain irregularity or imperfection in the arrangement of crystal structure, also known as crystal defects, is manifested in the phenomenon that the arrangement of particles deviates from the periodic repetition of the spatial lattice law in the local area of the crystal structure and appears disordered [26]. Based on the distribution range of disorderly arrangement, it is classified into three types: point defects, line defects, and plane defects (**Fig. 1**). Point defects (Zero dimensional defects) are deviations from the normal alignment of the crystal structure at nodes or adjacent microscopic regions. In other words, crystal defects involving only about one atomic size range in zero dimensions are indexed as point defects, including vacancies created by missing lattice atoms/ions in the lattice position; and doping induced by extra lattice atoms/ions filling the lattice gaps (**Fig. 2a**) [29, 30]. Specifically, in a crystal, when an atom has enough vibration energy to increase its amplitude to a certain extent, it may overcome the restriction effect of surrounding atoms on it, jump from its original position, migrate to the normal node position on the crystal surface or inner surface, and leave a vacancy inside the crystal, which is called Schottky defect (**Fig. 2a**). When the lattice is thermally vibrated, some atoms with enough energy leave the equilibrium position and squeeze into the lattice gap to form the gap atoms, while the vacancies are formed in the

original positions. This pair of point defects (vacancies and gap atoms) is called Frenkel defects (**Fig. 2a**).

When a vacancy is formed, in which an interstitial defect is created at the new position or the disappearance of the oppositely charged ions. For example, anionic and cationic vacancies have been demonstrated as functional active sites for a variety of materials [31-37]. Zou et al. introduced O vacancies by hydrogenation and verified that they could enhance the rate capability of $MAX@K_2Ti_8O_{17}$ as a sodium-ion anode material [37]. For doping defects, it is mainly divided into interstitial atom doping in which impurity atoms enter the gaps of the intrinsic atomic lattice, and substitution atom doping, in which impurity atoms replace intrinsic atoms [26]. When the charge of the foreign atom is different from that of the replaced atom, thus, the replaced atom will gain or lose electrons to reach charge equilibrium, and then, another vacancy or interstitial atom is produced (**Fig. 2a**). Therefore, heteroatom doping greatly influences the electronic structure of materials, improving the electrochemical performance [18]. In addition, when there are vacancies or tiny replacement atoms in the lattice, the surrounding atoms will move closer to the point defects, stretching the bonds between the surrounding atoms and generating a tensile stress field. When there are interstitial or large displacement atoms, the surrounding atoms will be pushed apart, resulting in a tensile stress field (**Fig. 2a**).

The actual crystal is subjected to the stress caused by impurities, temperature change or vibration during crystallization, or due to the mechanical stress of the crystal, such as blowing, cutting, grinding, *etc.*, the arrangement of the particles inside the crystal is deformed, resulting in the mutual slip between the atomic rows and columns. The one-dimensional defects formed by such crystals that do not conform to the ordered arrangement of the ideal lattice are called line defects. For example, edge dislocation, and screw dislocation (**Fig. 2b, c**) [38]. Among them, edge dislocation refers to a crystal surface with an extra half row of atomic surfaces in the upper half of the crystal, like a blade inserted into the crystal, resulting in atomic

misalignments between the upper and lower parts of the crystal surface (**Fig. 2b**). Unlike edge dislocations, a certain part of a crystal slips relative to the rest, the atomic plane spirals up along an axis, and the atomic plane rises by one interplanar spacing for each circle around the axis. At this time, the atomic disarrangement at the central axis is called a screw dislocation (**Fig. 2c**). Essentially, dislocation defects play a variety of roles in material mechanics, wherein they enhance the internal dislocation density through the activation of dislocation initiation and proliferation mechanisms. Since the dislocations in different slip systems are activated, the intersections between dislocations will also be increased due to the increment of dislocation density, significantly improving slip resistance and resulting in material hardening [39]. Furthermore, it is recently confirmed that dislocations greatly benefit Li transport channels by facilitating the insertion of Li ions, effectively increasing the reaction kinetics [40]. The possible reason is that atomic diffusion is a thermal activation process, and dislocations and other defects can significantly accelerate atomic diffusion due to their low activation energy under a lattice strain condition.

Planar defects are crystal defects that destroy the symmetry of an ordered alignment from a one-dimensional direction, including twins composed of two or more non-parallel regular conjoined crystals of the same type, grain boundaries composed by interfaces between grains of the same structure but different orientations, and stacking fault caused by introducing abnormal stacking atomic surfaces into normal stacking sequence (**Fig. 2d-f**) [41]. Under shear stress, crystal shearing occurs in a region in a continuous order along a certain crystal plane and crystal direction. As a result of deformation, the orientation of this part of the crystal is changed, but the deformed part of the crystal and the undeformed part of the crystal maintain a mirror symmetry relationship, and this symmetric mirror is called twin defect (**Fig. 2d**). Since the twin defect is an entirely coherent interface without distortion, thus the twin boundary has low energy and stable structure, which is highly stable in the field of energy storage and conversion [42, 43]. Stacking fault refers to surface defects caused by

introducing atomic planes of abnormal stacking order into normal stacking order, which mainly occurs in epitaxially grown crystals (**Fig. 2e**). Notably, the stacking fault does not cause lattice distortion, but due to the local destruction of the normal periodic arrangement of the crystal, stacking fault energy is introduced to increase the energy of the crystal, which can be applied as an active site for energy storage and conversion systems [22]. Grain boundaries are the interfaces between grains of the same composition and structure, mainly divided into high angle grain boundaries and low angle grain boundaries. Among them, the grain boundaries between grains in polycrystalline materials are called high-angle grain boundaries, that is, the grain boundaries with the potential difference of the high-angle grain boundaries of adjacent grains greater than 10 degrees [44-46]. However, the orientation difference between adjacent subgrains is less than 10 degrees, and the grain boundaries between these subgrains are called low angle grain boundaries, generally less than 2 degrees, which can be divided into inclined grain boundaries, torsional grain boundaries, overlapping grain boundaries, etc. (**Fig. 2f**) [44]. In addition, the characteristics of grain boundary are mainly as follows: 1. Large angle grain boundary has the highest grain boundary energy, so its grain boundary migration rate is the largest. Grain growth can reduce the total area of grain boundary and reduce the grain boundary energy, so grain growth is a process of energy reduction. 2. Many defects (dislocations, vacancies, *etc.*) at grain boundaries are conducive to atomic diffusion. 3. The solid phase transition occurs first at the grain boundary with high energy, so the grain boundary has a high nucleation rate. 4. High grain boundary energy results in higher grain boundary corrosion rate than inside grain.

2.2. Classification of crystal defects

To address the roles of crystal defects, characterization techniques relative to defect materials have been developed, which not only contribute to confirming the presence, type, and concentration of defects, but also provide direct proof to investigate coordination environment and local electronic states [7]. One is the spectroscopy strategy, which identifies

microstructural variations of materials by analyzing spectrogram signals. The other is micro-imaging, by which the microstructure of materials can be directly observed at the nanoscale or even the atomic level. In addition, the advantages, disadvantages and identification principles of specific characterization techniques are given in Table 1.

2.2.1. Electron paramagnetic resonance (EPR)

EPR spectroscopy is a powerful instrument for detecting the properties of unpaired electrons and surrounding structures [47]. Due to defects can trap electrons or holes, resulting in the occupation of unpaired electrons, inevitably causing to changes in the EPR signal [48]. Therefore, by analyzing the various g-values and signal intensities, information on the type of defect and its relative concentration could be acquired. Tian and colleagues introduced the disulfide (S_2^{2-}) and sulfide (S^{2-}) anion vacancies into the ZrS_3 nanobelts in a controllable strategy [49]. The EPR spectrum showed that the characteristic peak of $ZrS_{1-y}S_{2-x}$(15/100) is located at g = 2.0075, implying the presence of both S^{2-} and S_2^{2-} vacancies in this compound (**Fig. 3a**). Moreover, the signal intensity of $ZrS_{1-y}S_{2-x}$(15/100) is higher than that of $ZrSS_{2-x}$(15), indicating the presence of more sulfur vacancies in $ZrS_{1-y}S_{2-x}$(15/100). However, it is worth noting that numerous studies have ascribed the EPR signal with *g* factor 2.0023 to the electrons of the oxygen vacancies when demonstrating the existence of oxygen vacancies by EPR, but this explanation is not convincing due to the presence of *g* factor 2.0023 in other species, such as $^*OH$ radicals [50]. Thus, it is inaccurate to use EPR spectroscopy as the only evidence to confirm the presence of defects. It should be linked to additional techniques to further identify the presence of defects. Overall, the ultra-high sensitivity of EPR is an excellent technique for detecting low concentrations defects in electrode materials, but it may also cause misleading signals from other species.

2.2.2. Raman spectroscopy

Based on the principle that the Raman effect occurs when light irradiates the molecule and interacts with the electron cloud and molecular bonding in the molecule, the defect

structure of the material can be analyzed [51]. Specifically, defects alter the vibrational modes of the pristine hosts, manifesting as peak shifts, various vibrational enhancements, or new vibrational modes. The excitation of graphitic carbon by a light source with a wavelength of 325 nm produces two Raman signals: I_D and I_G. The I_D/I_G ratio in graphitic carbon is determined by Raman spectroscopy to obtain the defect concentration in the graphitic material [52]. For example, the increment of the calcination temperature of carbon leads to faster molecular thermal motion and, thus higher internal defect content, as evidenced by the increased I_D/I_G ratio in the Raman spectrum (**Fig. 3b**) [53]. Although Raman spectroscopic analysis of defects does not require sample processing to avoid the introduction of other defects in the processing process, the overlap and intensities of different vibrational peaks in Raman spectra are susceptible to the influence of the parameters of the optical system.

2.2.3. X-ray photoelectron spectroscopy (XPS)

By measuring the binding energies of specific elements using X-ray photoelectron spectroscopy, surface defect states and electronic information of electrode materials can be obtained [54]. This is because the presence of defects in electrode materials can alter the electronic structure and chemical environment of the constituent elements, resulting in peak shift, changes in intensity or the creation of new peaks. Xu et al. demonstrated that the introduction of defects could be characterized by XPS peak shifts [55]. Specifically, for the pristine MoS_2, the peaks of Mo $3d_{5/2}$ (at 229.7 eV) and $3d_{3/2}$ (at 232.8 eV) belong to Mo^{4+}, while the peaks of S $2p_{3/2}$ (at 162.5 eV) and $2p_{1/2}$ (at 163.7 eV) are attributed to S^{2-}. While for both Frenkel-defected (FD)-MoS_2-3 and Pt-MoS_2, the peaks in the Mo$3d$ and S$2p$ regions showed high binding energy shifts, respectively, suggesting the successful doping of Pt atoms into the MoS_2 lattice (**Fig. 3c, d**). However, sometimes the binding energy calibration of the electron is wrong in the XPS test, because it is a flawed method to calibrate the binding energy value with the C 1s peak of adventitious carbon [56, 57]. Specifically, it is suggested that the C 1s peak splits into two distinctly different contributions due to the C-C/C-H bonded

atoms of the accumulated indeterminate carbon layer on the Al and Au foils as a consequence of the vacuum level alignment at the adventitious carbon/ foil interface [57]. This finding exposed a fundamental problem with the reliability of XPS data, since the C 1s peak of adventitious carbon is often used for binding energy value calibration. However, there is no suitable method to replace it at present. Therefore, the researchers are also developing new calibration methods, such as the introduction of noble metal and gas atoms or the analysis of chemical states with reference to Auger parameters.

2.2.4. X-ray absorption spectroscopy (XAS)

Depending on the absorption range, XAS can be classified into X-ray absorption near edge structure (XANES) and extended X-ray absorption fine structure (EXAFS) [58]. The two methods provide complementary structural information, with XANES offering details of the electronic structure and coordination environment of the metal atom and EXAFS showing the type, number and distance of ligands [59]. Xiong and colleagues proved the existence of Ti vacancies by XAS analysis [60]. Compared with rutile TiO_2, the peak intensity of the pre-edge peak of $Ti_{0.87}O_2$ nanosheet increases in the Ti K-edge X-ray absorption near-edge structure (XANES) spectra, which indicates the reduced electron number of O 2p-Ti 4p hybridized orbital (**Fig. 3e**). This result shows the formation of unsaturated coordination O atoms, which is due to the existence of Ti vacancies. In addition, compared with rutile TiO_2, the Ti K-edge extended XAFS (EXAFS) k^3x(k) oscillation curve of $Ti_{0.87}O_2$ nanosheet shows a slight intensity decrease, and the intensity of the first major coordination peak corresponding to Ti-O bond in the Fourier transform Ti K-edge EXAFS data is significantly reduced (**Fig. 3f, g**). Both of these phenomena are strong evidence for the existence of Ti vacancies. It is worth noting that the XAS is mainly for an average assessment of bulky samples, which is unable to distinguish scattered atoms with a slight variation in atomic numbers. It is important to note that XAS is mainly used for the average evaluation of large samples and cannot distinguish between atomic information of similar atomic number.

2.2.5. Microscopic imaging characterization techniques

In addition to the above optical and electromagnetic characterization techniques of defects, advanced microscopy imaging characterization techniques are also essential. For example, a number of advanced visual instruments, such as high-resolution transmission electron microscopy (HRTEM), aberration correction transmission electron microscope (ACTEM), and scanning transmission electron microscope (STEM) with high-angle annular dark-field (HAADF), annular bright-field (ABF), and annular dark-field (ADF) can directly image the atomic structure of the sample and reveal the presence of defects. In addition, unlike spectroscopic characterization of defects, microscope imaging technology can directly distinguish point/line/plane defects and characterize the type of defects more correctly. For example, the $7.5Co_2P/Mn_{0.3}Cd_{0.7}S$ nanorods can be directly observed by TEM, and some obvious regular strip-like structures appeared, which was the typical feature of dislocation (**Fig. 3h**) [61]. Combined with a HAADF image, the atomic columns of the dislocations were labeled with blue spots (**Fig. 3i**). Additionally, red arrows represent dislocation regions according to the corresponding inverse fast Fourier transform (IFFT) patterns (**Fig. 3j**). Unlike dislocation defects, which exhibit linear misarrangements, vacancy defects in point defects show the disappearance of specific atomic sites. Take the sulfur vacancies in Ar-plasma-treated MoS_2 films as an example, there are four types of spots containing two S atoms (brighter and bigger dots), one S atom (darker and smaller dots), and spots without S atoms (totally dark), but no Mo vacancies (Mo removal), confirming the formation of S vacancies (**Fig. 3k**) [62]. While the data from microscopic imaging techniques can easily interpret and distinguish defect types, its main limitation is thickness, which must be thin enough to obtain a clear image.

2.2.6. Other characterization techniques

In addition to the defect characterization techniques detailed above, there are other methods (i.e., X-ray diffraction (XRD), positron annihilation spectroscopy (PAS),

photoluminescence spectroscopy (PL), and electron energy loss spectroscopy (EELS)) that can be applied as complementary methods to detect defects. These characterizations can also provide relevant indications about defect formation [63-66]. In general, various advanced techniques have unique features in characterizing crystal defects. However, certain complex defects are still difficult to accurately and completely identify, significantly when the material is enriched with many different types of defects. Therefore, it is desirable in the future to develop surface and bulk characterization methods to exploit the fundamental characters of defects at both in-situ temporal and spatial scales.

2.3. Simulations of crystal defects

Nowadays, it is still impossible to precisely control the concentration of crystal defects and determine their structure through experimental means. Thus, simulations provide another possible way to elucidate crystal defects in electrode materials. On the one hand, the critical components between crystal defect structure/other intrinsic properties and their electrochemical activity can be designed to guide the experimental synthesis of target electrodes. On the other hand, theoretical models provide information on adsorption energies and electronic structures, which are critical to understanding elementary reaction pathways in defect-rich electrode materials [67].

By comparing the adsorption energy and electronic structure of different theoretical models, the most favorable catalyst configuration was selected to accelerate the process of catalytic design. Based on periodic DFT calculations, whether the catalyst is more conducive to producing H_2O_2 or H_2O can be determined by the OOH* adsorption energy (GOOH*) function of the volcano plot [68]. Co has a higher oxophilicity and is therefore more prone to the cleavage of the OOH* intermediate to form H_2O. However, when electron-rich species such as O* are adsorbed near the Co N_4 moiety (CoN4(O)), the GOOH* increases from 3.9 eV to 4.1 eV, which is extremely close to the optimal value for H_2O_2 generation (**Fig. 4a**). In other words, Co N_4(O) retains most of its high catalytic activity and is more inclined to

produce H_2O_2. Based on this result, the Co_1-NG(O) catalysts obtained by using graphene oxide containing oxygen-rich functional groups to support Co single atoms are designed to have both extremely high activity and high selectivity in the process of electrochemical production of H_2O_2.

Based on the concept that the electronic structure of the collector can be provided by theoretical simulation, calculations show that the Fermi level of multi-vacancy defect-enriched carbon (MV) is much lower than that of bilayer graphene (BLG), indicating that the MV surface has a lower electronic energy level upon charging (**Fig. 4b**), which can alleviate electrolyte decomposition and prohibit SEI growth upon initial lithiation, thereby reducing the generation of inert lithium, enhancing the reversibility of galvanostatic cycling, and improving the cyclic stability properties of anode-free cells with a high areal capacity [69]. Dislocations affect adsorption energy in addition to changing the electronic structure [70]. On the one hand, the alloying of dislocation-strained IrNi alloy nanoparticles (DSIrNi) optimizes the electronic structure of the active site (Ir atom), resulting in the weakening of the Gibbs hydrogen adsorption free energy (ΔG_H) on Ir (**Fig. 4c**). On the other hand, the *d*-band center of Ir atom is shifted down to the Fermi level to fine-tune the electronic structure of the active site, which shows the same trend of weakening hydrogen binding energy (**Fig. 4d**). Interestingly, based on the simulation of the charge difference, strain effect and unique synergistic geometric effect of plane defects, calculations illustrate that the electronic structure and adsorption energy can also be ameliorated by plane defects, such as twin-rich copper, stacking fault-rich silver and grain boundary-rich gold [22, 71, 72].

3. Strategies for introducing defects

Solid, liquid, and gas are three typical forms of the existence of matter in nature. Since all crystal defects exist in solid state, solid-gas, solid-liquid, and solid-solid dual-phase interfaces are three typical systems in defect synthesis, which have been extensively studied in the synthesis of crystal defects. However, due to the increasing number of strategies to

manufacture defects, traditional methods of inducing defects tend to overgeneralize. To overcome this deficiency, four reaction methods for introducing defects were classified. Additionally, typical manufacturing defect strategies with their advantages and disadvantages are listed in Table 2.

3.1. Solid-gas reaction

Thermal redox of materials in the atmosphere is a simple and effective solid-gas reaction method to generate defects in electrode materials. The high temperature accelerates the movement of gas atoms, prompting the gas atoms to react with the solid electrode material, thereby forming point defects [29]. For example, in the atmosphere of NH_3, and O_2, it is a common method to introduce N and O doping defects to improve the electronic structure of carbon materials and thus enhance the electrochemical performance [18, 73]. Simultaneously, a versatile gas transport pathway has been demonstrated as a direct conversion of monolithic metal oxides into isolated single-atom electrocatalysts [74]. At elevated temperature, the surface metal oxides are initially vaporized to produce volatiles, which is then captured and reduced by the nitrogen-rich carbon support to form metal isolated single-atom sites/N doped carbon (MISAS/NC) catalysts (M = Cu, Mo, Sn) (**Fig. 5a**). Surprisingly, the proposed Cu ISAS/NC catalysts endow ORR with good catalytic activity in alkaline media, enabling high performance for Zn-air batteries [74]. In addition, the vapor deposition method is included in the solid-gas reaction for preparing electrode defects. Vapor deposition method is a technology that vaporizes the surface of material source into gaseous atoms or molecules under vacuum condition, and deposits some special functions on the substrate surface by means of low-pressure gas. For example, high nitrogen-doped bamboo-like carbon nanotube (B-NCNT) arrays were prepared by floating catalyst chemical vapor deposition (FCCVD) as metal-free catalysts for $Li-CO_2$ batteries [75]. B-NCNTs have high nitrogen content, particularly abundant pyridine nitrogen, and a unique periodic bamboo-like morphology with an abundance of defects and efficient active sites exposed on the surface, which endow them

with excellent catalytic performance. However, the vapor deposition technology also has some disadvantages, such as a low deposition rate of a few hundred nanometres per minute; In addition, both the reaction sources and the residual gases after deposition are flammable, explosive or toxic, so measures are taken to prevent environmental contamination and, in addition to the equipment, there is often a requirement for corrosion resistance.

3.2. Solid-liquid reaction

Under subcritical and supercritical hydrothermal conditions, because the reaction is carried out at the molecular level and the reactivity is increased, the hydrothermal reaction can substitute some high-temperature solid-phase reactions. Therefore, for solid-liquid reactions, hydrothermal reaction is considered to be one of the most commonly used methods due to its short time and uniform doping. Peng et al. successfully induced Co-doped defects into MnO_2 surface through the microwave hydrothermal method, which obtained a composite material with high electrical conductivity and plenty of hierarchical channels, resulting in accelerated CO_2 diffusion and suppressed electrode/electrolyte side reactions [76]. In addition to point defects, dislocations can also be generated in hydrothermal conditions. For example, MnOOH multilayer nanowires with high dislocation density have been successfully generated by a simple low-temperature hydrothermal method and investigated as anode materials for lithium-ion batteries [77]. As a result, the higher interlayer dislocation density ameliorates charge transfer and electronic conductivity, leading to excellent capacity retention and good cycling performance of the prepared MnOOH multilayer nanowires.. In addition, plane defects can also be formed in hydrothermal. Taking twinning as an example, adding $Pd(NO_3)_2$ and $Co(acac)_2$ to oleylamine, heating the reactor to 250 ℃ and finally injecting $AgNO_3$ solution into the mixture rapidly ,for 25 minutes, twinned Pd_2CoAg with vacancies can be obtained [78]. As a result, the surface charge density distribution can be adjusted by the synergistic effect of atomic vacancy and metal twin interface on the surface of Pd_2CoAg, and the ORR mass activity at 0.9 V is 5 times higher than that of Pt/C. Additionally, as the most

common method in liquid phase, acid etching is often used as a strategy to obtain vacancy-rich materials. For example, Ti vacancy-rich MXenes were obtained by etching in LiF/HCl solution at 35 °C for 24 h (**Fig. 5b**) [79]. The prepared potassium-philic MXene sheet can induce the nucleation of K, make K uniform deposition, avoid dendrite generation, and improve the performance of K negative electrode. However, hydrothermal reaction and acid etching are carried out in liquid phase, and water, as the most common solvent, often introduces -O/-OH functional groups into the material, thus affecting the performance of the material.

3.3. Solid-solid reaction

The most typical representative of solid-solid reaction manufacturing defects is the ball milling method. The imposed force during ball milling makes the solid materials collide with each other to introduce a large number of strains, defects, and nanoscale microstructures, which enables the easy and rapid preparation of defect-rich electrode materials [80-82]. Taking Fe, an active non-noble metal element commonly used in electrocatalysis, as an example, it is easy to produce nanoparticles with single twin and multiple twin structure defects under high plastic deformation in the ball milling process, which is caused by the reduction of crystallinity [83]. In addition, the greatly reduced particle size, the generation of numerous grain boundary defects and the generation of cold welding effects are caused by strong collisions during ball milling, which has been confirmed in the ball milling of silicon electrodes [84]. Specifically, the ground powders are nanostructured containing micron-sized agglomerates (median size ~10 μm), consisting of submicron cold-welded particles with a grain size of 10 nm. Besides, compared with typical nano-Si materials, the diffusion path of Li^+ is shortened by the presence of a large number of grain boundary defects, which enables the ball-milled Si nanoparticles to have a smoother phase transition during charge-discharge cycling. However, since the formation energy of point defects is smaller than that of plane defects, point defects are more common in the ball milling process than surface defects [80].

For example, the researchers manipulated the vacancies defect density and sp^2 cluster size in graphene by varying the ball milling time, while increasing the density of the material, resulting in a high defect content in graphene (**Fig. 5c**) [85]. As the main storage site in electrochemistry, the vacancies defect can store sodium through the rapid reversible process of sodium ion adsorption and desorption, and exhibit capacitive storage behavior. Unfortunately, the high temperature and high pressure in the tank can only be generated by extremely high ball milling process speed, which has disadvantages such as high energy consumption, long preparation cycle, etc., and at the same time, solid impurities from grinding media and grinding tanks are easily introduced into the final product [86]. Additionally, a large amount of material waste is caused by the cold welding effect in the ball milling process, which increases the synthesis cost. Although adding grinding aids such as n-hexane can effectively prevent the cold welding effect, most grinding aids have high toxicity, threatening the safety of researchers [87].

3.4. Other reactions

Plasma-assisted (PA) etching methods have received increasing attention due to their distinctive "species response characteristics" and wider and adjustable operating requirements [88]. Plasma, in short, is an aggregate of ions, excited atoms, ionized atoms/molecules, free electrons, and free radicals (not a solid, liquid, or gas), which are derived from ionized gases by providing sufficient energy [89]. Within the plasma, the main chemical reactions are based on free radical chemistry, and the unique properties of which are ascribed to the physicochemical equilibrium property of electrons [90]. The generation of defects by the plasma etching strategy can be ascribed to a fundamental collision mechanism [90]. Firstly, in the presence of a strong electric field, the high-energy species in the plasma system constantly attack the surface of the material, leading to the destruction of the surface structure, the fracturing of chemical bonds with lower bond energies and the removal of excess reactants, ultimately leading to the effect of creating defects. Subsequently, defects on the surface of the

electrode material further interact with other radicals or ionized atoms/molecules to create new relatively stable chemical bonds or elemental states, resulting in heteroatom doping, surface modification and functionalization, which affect the performance of the electrode material. For example, CHF_3 plasma etching method is used to prepare MoS_2 active edge sites in large quantities while conducting controlled fluorine doping on the edge sites (**Fig. 5d**) [91]. However, despite many recent studies utilizing plasma to fabricate defect-rich electrode materials, it is difficult to understand the exact role of free radicals, electrons, and ions in plasmas in creating defects due to the physicochemical complexity and non-equilibrium thermodynamic properties of plasmas [90].

Light irradiation can induce a variety of electron and molecular movements, but light does not belong to any of the solids, liquids, or gases. As a non-contact manufacturing tool, the irradiation process is accurately regulated, permitting the heating of specific parts to actuate the reaction at the required position to produce defect-rich structures in a highly controlled manner [92]. In comparison to the conventional reaction environment generated by classical strategies, a surge in temperature is usually expected when the focused laser beam hits the intended region, followed by rapid cooling as the irradiation stops [93]. Unique reaction conditions are created by this rapid heating and cooling, which facilitates the directly preserve structural defects in the final product, such as the formation of heptagons and pentagons in graphene's hexagonal lattice [94, 95]. Local surface charges can be caused by these inherent carbon defects, and these defects can act as, storage, adsorption, or activation sites for external species during electrochemical processes. Taking advantage of this property, the researchers fine-tuned the in-plane porous structure of GO to produce nanocarbon suspension bonds by adjusting the laser energy or time, allowing the metal species to be extracted from the bulk metal under environmental conditions and transformed directly into a single atomic structure [96]. This method not only greatly reduces the synthesis cost and the lowest energy consumption, but also helps to maintain the structural integrity of the GO

matrix and prevent the electrical conductivity of the catalyst from being affected. In addition to carbon materials, metal nanocrystals and metal compounds can also introduce defects using similar principles to effectively load single metal atoms or directly catalyze reactions [31, 97]. For example, the unique characteristics of ultrafast laser, ultrahigh intensity, and ultrashort pulse duration result in the formation of defects and metastable CeO_x species on the CeO_2 support surface (**Fig. 5e**) [98]. Simultaneously, the metastable CeO_x migrated to the Pt particles under the induction of laser, forming a discontinuous porous coating layer with a thickness of several atomic layers. Due to the porous nature of the defection-rich coating, the catalyst has better catalytic activity and stability. However, as an emerging method for defect preparation, laser-mediated precise structural modulation mechanism of materials is still controversial [93]. Photothermal and photochemical effects and their combinations are difficult to explain the unique processing of materials.

4. Defect regulation of energy materials

4.1. Point defect

4.1.1. Doping

Heteroatoms doping in energy storage and conversion systems is considered as extremely critical CDE. After heteroatoms doping, the density of states, electronegativity and charge distribution of electrode materials will change fundamentally, which tunes the physicochemical properties and composition of electrodes and provides low kinetic and thermodynamic pathways for electrochemical reactions [76, 99]. Theoretically, the electronegativity difference between heteroatoms and carbon atoms is favorable to form electronegative centers to adsorb lithium ions (**Fig. 6a**) [100]. The formation of "local dipole" is beneficial to further enhance the ion-dipole interaction between lithium ion and nucleation site. Charge transfer is one of the necessary conditions to reduce the lithium barrier confirmed by the in-situ etch the MAX phase (Ti_3SiC_2) to form S-F co-doped carbon (SFC5) [53]. As shown in **Fig. 6b**, the positive binding energy of Li to carbon demonstrates that Li interacts

loosely with pure graphene (0.8068 V). However, when the S/F heteroatoms are doped, the interaction between the adsorbent and the substrate increases, indicating that the lithiophilicity of the S/F co-doped defective carbon is enhanced. In addition, as shown in **Fig. 6c**, the charge transfer from lithium to D-SF-1 of SFC5 is more pronounced than that to pure graphene, which is evidenced by the delocalized electron in-between the conjugation structure. Finally, Symmetrical batteries equipped with SFC5 are able to operate stably over a wide temperature range and possess the lowest overpotential compared with other batteries (**Fig. 6d**).

Single-atom doped catalysts have recently been studied in electrocatalytic reactions due to their excellent atomic utilization, high catalytic activity and selectivity [86]. A convincing example is the preparation of novel Zr-N/O-C catalysts by ball-milling solution-assisted pyrolysis **[18]**. As shown in **Fig. 6e**, high-energy ball milling can induce high temperature and high pressure, which is sufficient to reorganize Mg and Zr atoms and form MgZr alloys, resulting in Zr-N/O-C after further calcination and acid etching as observed from the TEM image (**Fig. 6f**). Compared with ZrN_4, the charge depletion on the Zr of unsaturated dual-ligand confining ZrN_4O structure is more evident, resulting in a lower electron population on the metal. (**Fig. 6g, h**). Therefore, the ZrN_4 is located in the region with poor adsorption energy, while the ZrN_4O structure is close to the optimal center with better binding energy of reactants. However, the single atoms easily cause migration agglomeration, and the loading content of dopant atoms is extremely low, which leads to poor durability under harsh conditions [101].

4.1.2. Vacancies

The atoms located at the lattice points in the crystal are constantly thermally vibrating at their equilibrium positions. At any moment, some atoms' energy is large enough to overcome the binding of surrounding atoms to them, thereby leaving their original equilibrium positions and migrating elsewhere, and vacancies appears in the original position. Removal of a positively charged atom from the normal lattice position in the crystal results in an anion

vacancy, whereas removal of a negatively charged atom results in a cation vacancy. Cation vacancies and anion vacancies can potently tune the electronic properties of electrode materials, thereby facilitating redox reaction kinetics and charge transfer. Additional host sites for intercalated protons or cations can also be served by these defects, facilitating ion diffusion during electrochemical cycling [26]. Among them, anion vacancies are the most widespread intrinsic defects, such as oxygen vacancies. For example, oxygen vacancies are introduced by a hydrogenation process, which modifies the $K_2Ti_8O_{17}$/Na surface state (**Fig. 7a**) [37]. As a result, the electrical conductivity of the MAX@$K_2Ti_8O_{17}$ core-shell structure composite was greatly improved, and thus the rate performance of the composite was maintained at 75 mAh g^{-1} after 10,000 cycles at a rate of 10 A g^{-1} (**Fig. 7b**). Experimentally, the single S vacancies of MoS_2 (MoS_2-EGMO) can optimize the surface electronic structure, which is facilitated to the adsorption of hydrogen on the surface of MoS_2, thus adding more active sites on the inert basal plane (**Fig. 7c, d**) [19]. Different from another classical vacancy defect, cationic vacancy is rare, probably due to the lack of suitable matrix materials [26]. For example, introducing a Ti vacancy into the nitrogen atom-containing MXene layer can significantly enhance the binding energy between MXene and K atoms (**Fig. 7e, f**) [79].

Finally, the synergistic effect of anion vacancies and cation vacancies to improve the performance of electrode materials has also been reported [17]. A convincing result is that in MXene-derived TiO_2, the defect structure can be stabilized by Ti vacancies, thereby improving the reducibility of lattice oxygen and lowering the activation energy barrier of ethane, while the activation of O2 and recovery of lattice oxygen is due to the presence of O vacancies [17]. Theoretical calculations show that better electronic conductivity and lower ionic diffusion energy barrier can be obtained through the introduction of cation vacancies; However, experimental measurements of more detailed structure and oxidation state changes are still required to further correlate the process of charge storage with intentional cation vacancies.

4.2. Line defect

4.2.1. Dislocation

The formation of dislocations in the crystal is divided into two situations: 1) The irregular arrangement of one or more rows of atoms in a crystal leads to the formation of dislocations. 2) Generation of dislocations due to the movement of defect lines perpendicular to the direction of stress and atomic displacement [40]. Unlike point and planar defects, dislocations are easily generated by strain or thermal process control [20, 102]. A non-equilibrium high-temperature thermal-shock method (HTS) to induce dislocations in nanocrystals by using liquid nitrogen has been reported (**Fig. 8a**) **[20]**. The dislocations induced by thermal and structural stress are frozen in nanoparticles (**Fig. 8b, c**). Furthermore, the high-energy surface structure generated by dislocations can prevent surface reconstruction during the catalytic process and improve its hydrogen evolution reaction performance (**Fig. 8d**) [103, 104]. In contrast, researchers have also found that dislocations can enhance the ion mobility and promote the insertion of lithium ions into the crystal to effectively improve the reaction kinetics [40, 105]. The transition metal oxide-Co_3O_4, whose practical application is limited by the shortcomings of the conversion reaction, the slow kinetics of lithium ion transport and the drastic volume change after long-term cycling seriously affect the practical application of commercial pure Co_3O_4. In turn, the synergistic effect of edge dislocations and crystal planes is observed in the modified Co_3O_4, providing a good buffer band for unprecedented electrochemical behavior with high specific capacity, excellent cycling stability, and superior high-rate performance [105]. Additionally, lithium nucleation is affected by changes in the dislocation density in the current collector. Lowering the nucleation barrier and promoting the uniform nucleation of lithium can be caused by the increment of dislocation density [102]. As shown in **Fig. 8e, f**, the binding energy of lithium for the strained copper foil with dislocation is higher than that of the copper foil without dislocation. Furthermore, the homogenization of nucleation behavior can be promoted by the

increase of dislocation density, resulting in nuclei being steadily grown above the critical radius, and large nuclear sizes and low nuclear densities being formed.

Although many defects are formed by dislocations at the crystal structures, providing abundant active sites for storing ions, numerous researchers have believed that large dislocation structures with strain and stress are generated through severe volume changes, leading to fracture and comminution of electrodes s [103, 106, 107]. For example, the dislocation cloud gradually propagates along the SnO_2 nanowires, causing the nanowires to swell, elongate and helicate upon charging observed by Huang et al. Therefore, it remains a challenge to create a large number of active sites and suppress severe volume expansion by controlling the dislocation density. In addition, dislocations are more easily formed in lithium-rich layered oxides than in conventional layered oxides, suggesting that the formation and evolution of dislocation defects are related to voltage decay [108]. However, there are currently few techniques for dynamic characterization and observation of dislocation defects. Therefore, the development of technology to observe the nucleation and evolution of dislocations in electrode materials is one of the future directions in the field of defect research.

4.3. Plane defect

4.3.1. Twin

In contrast to point defects, the distribution of planar defects has less homogeneous, and it is largely influenced by the variation of the thermodynamic state [41]. Twin boundaries are the simplest type of plane defects. The twinning relationship refers to the orientation relationship in which two adjacent grains or two adjacent parts within a grain form a symmetrical mirror relationship along a common crystal plane. The atoms on the twin boundary are located at the junction of the two crystal lattices at the same time, and are shared by the two parts of the twin. [42, 109, 110]. The properties of materials are significantly affected by the presence of twin boundaries, such as the improvement of tensile and

compressive properties, thermodynamic stability, electromigration resistance, *etc*. [111]. Twin boundaries with low interfacial energy are considered to be one of the most stable defects in typical face-centered cubic metals [112]. For example, the quintuple twinned silver obtained by direct reduction of $AgNO_3$ by the reductive nature of alkaline intercalated MXene solutions possesses intentional ORR catalytic performance [113]. Specifically, the formation of Ag seeds was induced by the addition of PVP solution, and then Ag/Ti (Ag0.9Ti0.1) bimetallic nanowires were generated (**Fig. 9a, b**). The four-electron transfer process is facilitated by the unique five-twinned Ag-rich bimetallic nanowires with high current density and great stability, which results in a large number of oxygen adsorption sites being provided and the diffusion path of adsorbed oxygen being shortened. In addition, the atom-specific activity of the twin-boundary edges is not significantly different from that of the single-crystal edges formed from the crossing of two (100) surfaces, and it shows two orders higher activity than the silver nanocubes (100) surface (**Fig. 9c, d**) [114]. Nevertheless, the catalytic effect of twinned silver structures is often influenced by factors such as strain, size effects and capping agents. So, it remains challenging to reveal the catalytic role of the twin boundary under definite conditions. To eliminate unnecessary factors in the nanocatalyst, high-density silver's twin boundary (twin density is $1.5 \times 10^4 \text{ cm}^{-1}$) on a flat graphene film using the current pulse deposition technique. Driven by these twin boundaries, the electrocatalyst effortlessly transfers electrons to CO_2, resulting in direct electrosynthesis of 52% concentrated CO_2.

High temperature thermal shock strategy, as a non-equilibrium solid-phase preparation strategy, can successfully complete the rapid heating and cooling process of electrode materials in an extremely short time, which allows the entire nucleation and growth process of crystals to be controlled in an instant, resulting in the intercession of twin defects in the crystal [43]. Molecular dynamics simulation results show that under non-equilibrium conditions, the twinning of Pd nanoparticles is dominated by rapid cooling, and the particle size is positively correlated with the twin boundary density. Consequently, the binding of CO

and OH at different surface sites can be altered by the presence of TBs, resulting in heterogeneous adsorption of CO on the surface while enhancing the adsorption of OH (**Fig. 9e**), enabling the carbon electrode material composed of twinned structure with the best EOR catalytic effect compared to twin-free Pd/C and commercial Pd/C (**Fig. 9f**).

However, the liquid-phase synthetic route is considered as the main strategy for the synthesis of TBs, which obtains TBs by adjusting specific synthetic conditions or reagents to control the reaction kinetics (such as reduction, nucleation, or growth). [115, 116]. Additionally, the agglomeration of particles and/or impurities associated with reagents is the most significant challenge. Currently, the preparation of abundant TBs by solid-phase synthesis is limited by the slow reaction rate. Therefore, it is considered of great significance to introduce crystal surface defects directly into the nanostructures by solvent-free assisted strategies. Such as the high temperature thermal shock strategy described above, this emerging non-equilibrium solid-phase preparation strategy can successfully complete the extreme heating and cooling process of electrode materials in a short time. Compared with the traditional mild liquid phase, near-equilibrium preparation strategy, the period is extremely short, resulting in numerous twinned defects in the material.

4.3.2. Stacking fault

Stacking faults inside crystals are introduced by changing the stacking order of metal atoms, thus introducing multiple stepping positions, as shown in **Fig. 10a, b [22]**. As the periodic crystallinity of these sites is disrupted, resulting in changes in the surface atomic coordination numbers and electronic structure of the crystal (**Fig. 10c**). Hence, interaction and adsorption with the intermediates and reactants can be intrinsically regulated, thus improving catalytic performance (**Fig. 10d**). Unexpectedly, the intrinsically inactive nanometallic crystals, such as silver (Ag) nanoparticles, can be tuned to become powerful HER electrocatalysts when stacking faults are introduced (**Fig. 10e, f**). Additionally, as shown in **Fig. 10g**, stacking faults with the fault vector b/6[110] were observed during the delithiation

of Li_2MnO_3 [117]. The low mobility of the stacking faults contributes minimally to the release of oxygen from the structure and promotes reversible redox reactions. In contrast, another type of defect (Burgers vector for c/2[0 0 1] of dissociative dislocations) due to its higher sliding mobility, dissociative dislocations lead to the formation of oxygen-associated species and assist in the transport of oxygen-associated species to the electrode surface, resulting in the irreversible formation and release of O_2 gas (**Fig. 10h**).

However, stacking faults can also have negative effects on electrode materials. A classic example has been shown that stacking faults hinder lithium intercalation in Li_2RuO_3 [118]. Specifically, the formation energy difference between Li_2RuO_3 with and without stacking faults structure has little effect on the thermodynamic delithiation potential. Stacking faults exhibit a "labyrinth effect" on Li intercalation in layered oxides, resulting in severe first-cycle capacity loss. As a result, the back-intercalation of Li^+ is hindered due to the large number of residual stacking faults in the low delithiation state and the newly generated stacking faults during the discharge process, resulting in the low first-cycle Coulombic efficiency of Li_2RuO_3.

Therefore, it is necessary to visualize stacking faults and correlate the existence of stacking faults with incomplete phase changes in positive electrode materials to understand the relationship between significant abnormal capacity loss of cathode materials and the evolution of stacking faults. This will provide a new idea for the design of new cathode materials and improve the performance of existing materials by adjusting stacking structure or reducing stacking fault defects.

4.3.3. Grain boundary

The junction between the different crystal orientations in a crystal is called grain boundaries (GBs) [84, 119]. The lattices along these boundaries is to a large extent distorted. The resultant local strain provides highly active surfaces with optimized electronic structures for catalysis. Taking Au nanoparticles (NPs) as an example, the surface density of grain

boundaries on Au NPs decreases by increasing the annealing temperature [72]. Moreover, the monotonic increment of the CO2 reduction reaction (CO$_2$RR) current density varies with the total GB surface density. However, the HER activity did not correlate with the GB surface density. These two phenomena confirm that the presence of GBs in Au NPs is quantitatively correlated with the electrocatalytic activity of electrochemical CO$_2$ reduction, but not with HER activity (**Fig. 11a**). To clarify the selective catalytic phenomenon of GBs region on Au electrode, the effect of GBs with large grain size on flat polycrystalline Au electrodes was further investigated. This effect was observed by scanning electrochemical microscopy to be due to a selective increase in CRR activity at the terminations of the grain boundaries (**Fig. 11b, c**) [72]. Furthermore, the width of the active enhancement region depends mainly on the geometry of the GBs, which determines the concentration of dislocations in the GBs region. Nonetheless, the mechanism behind this process is still unclear, and the structure-activity relationship cannot be precisely constructed. Therefore, the same group used electron backscatter diffraction (EBSD) combined with scanning electrochemical cell microscopy (SECCM) to study bulk defects on gold surfaces (**Fig. 11d-f**) [120]. The results show that the improvement of the above selective catalytic activity comes from the increase in the number of coordinately unsaturated atoms at the grain boundaries (**Fig. 11g-j**). Specifically, the uncoordinated sites are considered to be the most active sites for CO$_2$ reduction, and the dislocation density can be enhanced at GBs where dislocation migration is hindered. This phenomenon is attributed to step nucleation at the termination of the dislocation surface, which changes the number of uncoordinated sites. Comparatively, the HER does not depend on uncoordinated sites and does not exhibit an enhancement in the rate of hydrogen evolution at these sites.

Due to the high activity of grain boundaries, it can also negatively affect the electrode material. For example, typical polycrystal Li$_{1.2}$Ni$_{0.2}$Mn$_{0.6}$O$_2$ will have a significant volume change (2.34%) in the process of Li$^+$ de-intercalation, which will cause serious cracks in its

particles during long-term cycling, and the electrolyte will enter the inside of the cathode particles along the cracks and cause secondary reaction, further reducing the cycling performance of the material [121]. In contrast, single-crystal Li-rich $Li_{1.2}Ni_{0.2}Mn_{0.6}O_2$ can effectively suppress this volume change (1.47%) with almost no cracks during cycling, thus exhibiting more stable cycling performance. Moreover, since the majority of synthetic solid electrolytes are polycrystalline, GBs have an unavoidable effect on their properties [122, 123]. For instance, many studies have demonstrated that the resistance at GBs is associated with a decrease in ionic conductivity in solid electrolyte [124, 125]. In addition, GBs may promote the growth of Li dendrites in solid electrolyte, resulting in short circuit of the cell [126, 127]. Heterogeneous depletion of GBs and low ionic conductivity are reported to be responsible for dendrite growth [128]. Especially, recent studies have proposed that dendrite propagation results from high electron conductivity, which appears in GBs [129, 130]. To fully unravel these serious GBs problems requires a comprehensive understanding of the ionic diffusion, defect chemistry, and electronic properties of GBs. In particular, the Li-ion conductivity of GBs was revealed using classical simulation methods [123, 131]. First principles simulations based on atomic models are a forceful tool to provide comprehensive studies on the properties of solid electrolytes. It has been widely used to explain phase transitions [132], migration mechanisms [133], electrochemical windows [134], crystal defects chemistry [135], and surface and interface phenomena with lithium metals [136]. Unfortunately, there is still a lack of research on major GBs problems in solid electrolyte based on first-principle simulation, which is also one of the research directions of grain boundary defects in the field of energy in the future.

5. Summary and Outlook

CDE is recognized as a powerful method to enhance the efficiencies of electrochemical energy storage/conversion technologies. At present work, we mainly summarized and discussed the strategies for generating defects, the methods of defect characterization, the

classification of various defects and their effects on the electrochemical performances of electrode materials. As listed in the Table3, 4, the preparation methods of electrode materials become more and more abundant in terms of defects in the field of catalysis or batteries in the last decade. Theoretically, the generation of defects requires a large amount of energy to cause atoms in material to detach or move to other positions, such as high temperature to accelerate atom movement, laser irradiation to promote atomic transition, strong plastic deformation of ball milling to change the crystal structure, and strong etching of plasma to change electrode composition.

In addition, according to the second law of thermodynamics, defects in crystalline materials are considered essential [137]. And the type of defect is also affected by thermodynamics, taking vacancies as an example, double vacancies can be created either by the coalescence of two single vacancies or by removing two adjacent atoms. In addition, there are no dangling bonds in the fully reconfigured double vacancy, so that instead of four hexagons, two pentagons and an octagon appear in the perfect graphene. In the case of slight perturbations of the bond lengths around defects, the atomic network remains coherent. The simulation results show that the formation energy Ef of double vacancies is of the same order as for single vacancies (about 8 eV). The current absence of two atoms results in each missing atom having a much lower energy than the individual missing atoms [138, 139]. Therefore, double vacancies are thermodynamically favored over single vacancies.

Generally speaking, according to the nature of crystal defect engineering, the main roles of defects in energy storage and conversion systems can be summarized as follows (**Fig. 12**): I). Crystal defects can be exploited as energy storage/adsorption/active/nucleation sites. II). Defective sites can reduce the thermodynamic energy barrier for electrochemical reactions. III). Crystal defects can enhance the electron conduction rate and activity of electrode materials. IV). Crystal defects facilitate the rapid diffusion of ions inside the electrode materials. V). Crystal defects can be used to adjust the charge density distribution.

With the rapid development of material synthesis technology, the role of CDE in electrochemical energy storage and conversion systems has gradually been attracted more and more attention. However, there are still lots of unsolved scientific and engineering issues. Firstly, in comparison to point defects, the researches on line defects and plane defects are very rare, dependent on traditional synthesis processes (**Fig. 13**). Noticeably, these two defects have many advantages in electrochemical energy storage, such as extremely fast ion diffusion. More recently, defect preparation methods under extreme conditions, including high-temperature pulse, laser irradiation, high-energy ball milling and plasma bombardment, can be regarded as a possible method to tune linear and planar defects, which pave some new paths to achieve one dimensional or two dimensional defects in the future.

Secondly, defect synthesis in electrode materials is generally considered to be uncontrollable so far, and it is still a great of challenge to attain of certain single type of defects (**Fig. 13**). Appropriate preparation techniques are desirable for obtaining more exposed active sites. Also, it is difficult to distinguish defect synergistic effects of many complex defect types in electrode materials. The combination of advanced performance testing methods and microscopy techniques has gradually attracted the attention of researchers. However, transport blockage of electrode materials, and even structural degradation or collapse may be caused by excessive defects. Thus, quantified or customizable direction to design electrode material through CDE is the trend of future research. Therefore, reasonable defect concentration and controllable defect structure have been considered as important strategies to enhance the electrochemical performance of electrode materials.

Thirdly, defect-rich electrode materials rarely meet the practical needs of industrial production (**Fig. 13**). Therefore, methods for large-scale fabrication of defective electrode materials must be further researched and developed. There are two main directions as follows: 1. The improvement of the synthesis efficiency and yield, such as simplifying the experimental process for fabricating defect-rich electrode materials. 2. The reduction of the

noble metal utilization rate, such as reducing the proportion of noble metal atoms doping defects, so as to improve the utilization rate of noble metals in catalysis.

Fourthly, the specific reliable mechanisms of crystal defects in electrode materials remain vague, due to the absence of advanced characterization techniques (**Fig. 13**). At present, ex-situ electron microscopy is still the main method for defect identification, which can achieve the observation of a certain state of electrode material, but cannot monitor the dynamic change of defects in the electrochemical cycle. Therefore, more advanced electron microscopy detection strategies, especially in-situ measurement techniques (such as in-situ transmission electron microscopy), are the critical to further differentiating the variation of defects in electrochemical reactions in order to gain more insight into the reaction mechanisms of defects in electrode materials. Besides electron microscopy, spectroscopy is also an important tool for measuring defects, which can be used to measure the concentration and type of defects by optical signals without complex pretreatment of samples. However, single spectroscopy often has limitations in measuring defects and may generate bias or even erroneous information (such as misjudgment caused by the overlap of Raman peaks, deviation caused by the binding energy of C 1s peak calibration in XPS). Therefore, the accuracy of the results can be ensured by mutual verification of various spectral measurement methods. In addition, the development of in situ spectroscopy is still the future trend, so that the changes of defects in the electrochemical process can be better detected to determine the action mechanism of defects in the reaction.

Fifthly, the application of electrochemical measurement is a necessary means to prove that defects have good performance (**Fig. 13**). These electrochemical measurements focus on what changes in electrochemical properties are induced by the defects. Certainly, electrochemical measurements are the most intuitive representation of the effect of defect-rich electrode materials on performance. For example, Shi et al. showed that in $MoSe_2$ with N doping (DN) and Se vacancy (VSe), N doping significantly reduced the Tafel slope of the

peak representing the nucleation of Li$_2$S, while further merging of Se vacancy seriously reduced the dissociation peak of Li$_2$S [140]. Since a smaller Tafel slope implies a faster electrokinetic process, it can be confirmed that DN and VSe selectively accelerate the nucleation and dissociation reactions of Li$_2$S. However, electrochemical measurements often only show the changes in the electrochemical performance of the defective electrodes, but do not provide a mechanistic explanation. Therefore, it is necessary to combine the characterization techniques and theoretical calculation of the mechanism analysis, so as to clarify how the defects enhance the performance of the electrochemical system.

In addition, the application of theoretical guidance from computational simulations in defect electrochemistry has greatly facilitated the development of novel defect-rich electrode materials (**Fig. 13**). The theoretical guidance results of these computational simulations are mainly focused on predicting defects as new active sites or verifying of defect-induced changes in electrochemical properties [141]. Undoubtedly, the theoretical guidance of these computational simulations has certain guiding significance for the design of high performance defect rich electrode materials and the deep understanding of defect electrochemical mechanism. On the one hand, it provides a feasible method for determining the true active centers of electrochemical energy storage and conversion systems. For example, Zhang et al. obtained insights into various defects (including topological defects and heteroatom doping) through DFT simulations and revealed the defect structure-electrochemical activity relationship based on DFT calculations and electrochemical measurements [142]. On the other hand, the combination of DFT simulations and electrochemical measurements can elucidate a wider range of guiding principles, enabling further understanding of various electrocatalytic mechanisms and energy storage mechanisms.

In conclusions, the impacts of CDE on electrode materials have been confirmed as an irreplaceable trajectory to enhance electrochemical properties in the energy storage and conversion fields. In this regard, it is desirable to perform abundant works in related to CDE.

Herein, this review provides a profound understanding and enlightenment on the design/mechanisms of advanced defect electrode materials, which plays an essential role in accelerating the development of the electrochemical energy storage and conversion industry in terms of this new strategy.

Declaration of competing interest

The authors declare that they have no known competing financial interests or personal relationships that could have appeared to influence the work reported in this paper.

Acknowledgments
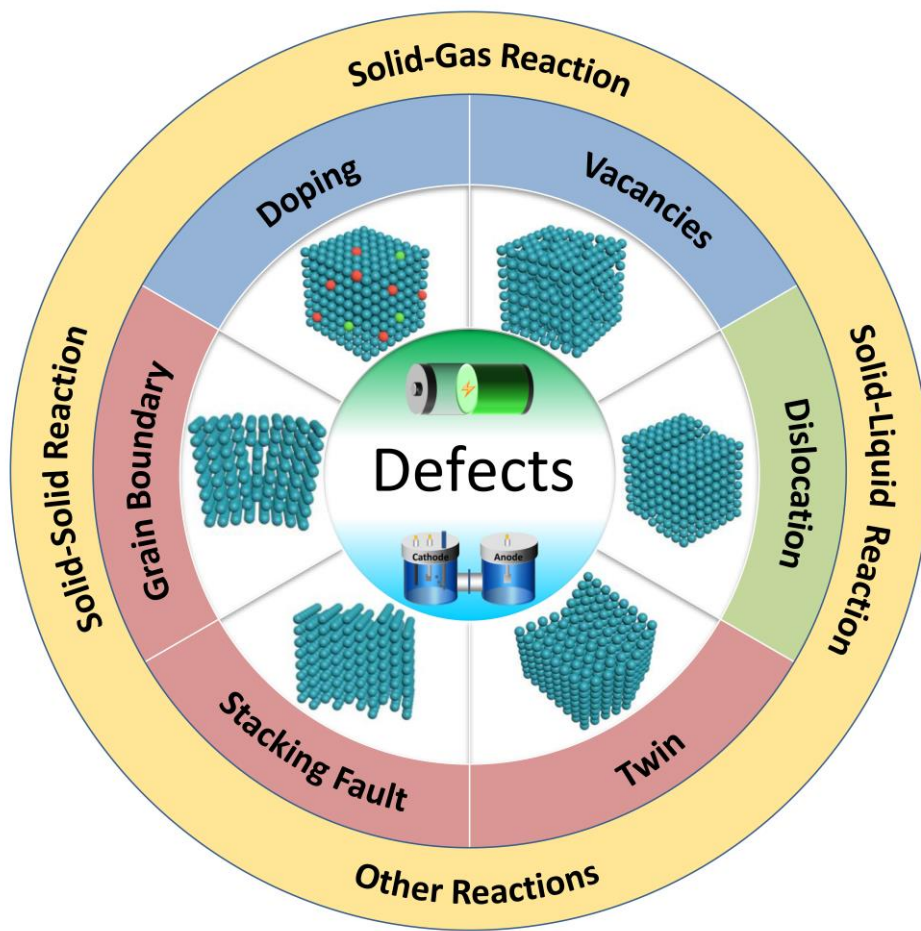
Fig. 1 Illustration of CDE in the battery and catalytic systems.
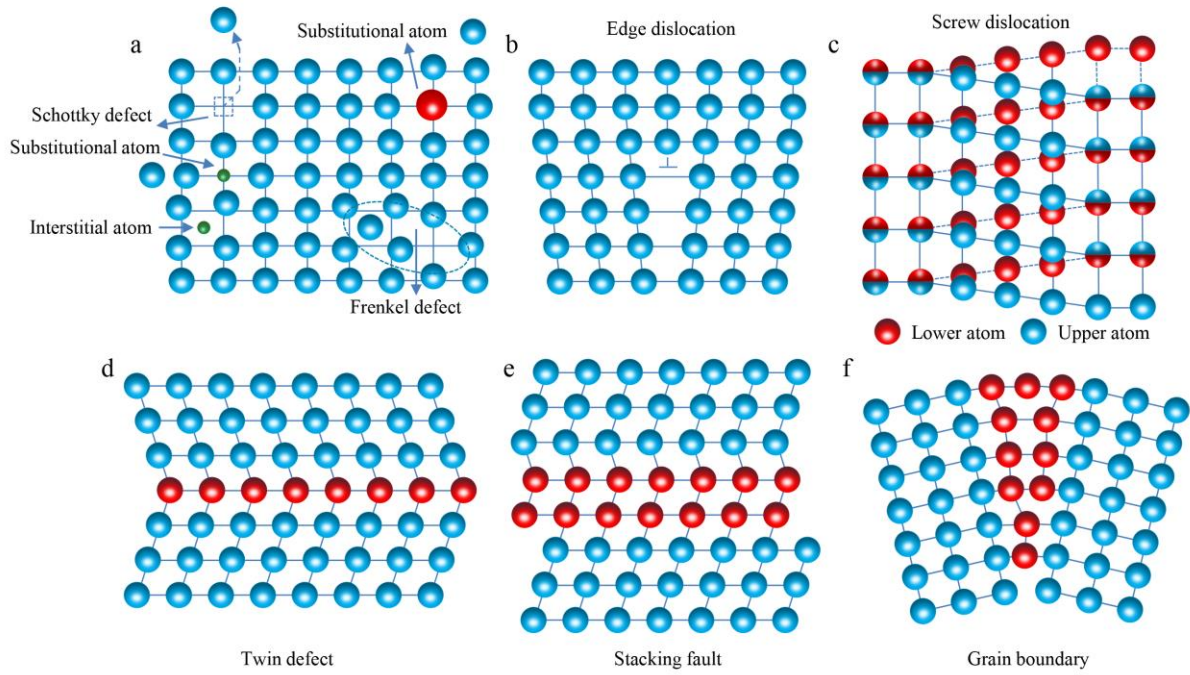
Fig. 2 Schematic illustrations for the different types of crystal defects. (a) point defects include doping and vacancies; (b-c) line defects include (b) edge dislocation and (c) screw dislocation; (d-f) plane defects include (d) twin, (e) stacking dislocation and (f) grain boundaries.
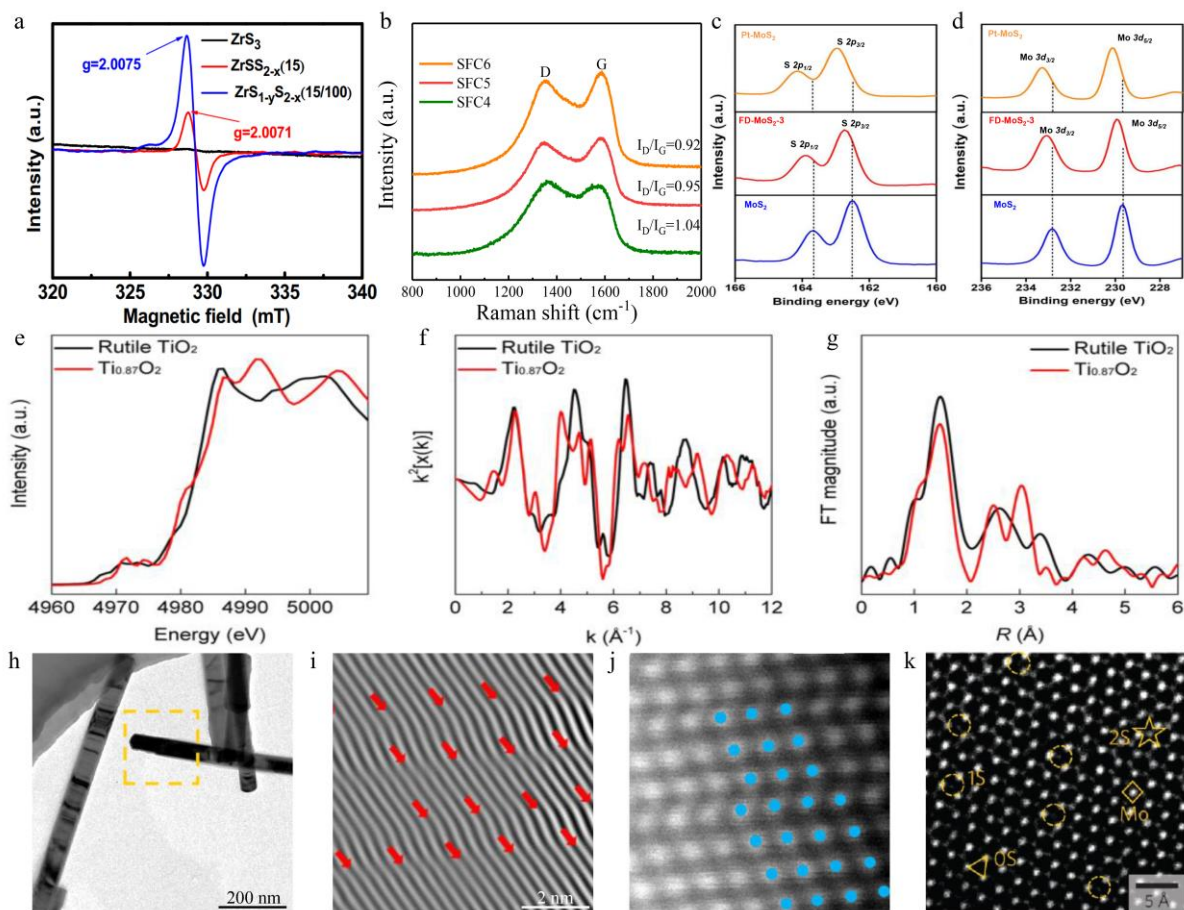
Fig. 3 (a) EPR spectra of the ZrS_3, $ZrSS_{2-x}(15)$ and $ZrS_{1-y}S_{2-x}(15/100)$ NBs [49]. Copyright 2021, Springer Nature. (b) Raman spectra of the SFC4, SFC5, and SFC6 [53]. Copyright 2022, Elsevier. (c, d) Deconvoluted S 2p and Mo 3d spectra of pristine MoS_2, FD-MoS_2-3 and Pt-MoS_2 [55]. Copyright 2021, Springer Nature. (e) X-ray absorption near edge structure (XANES) of Ti K edge, (f) the k3-weighted EXAFS in K-space and (g) Fourier transforms of k-space oscillations of Ti K edge of rutile TiO_2 and $Ti_{0.87}O_2$ [60]. Copyright 2021, Springer Nature. (h) TEM images of 7.5Co_2P/$Mn_{0.3}Cd_{0.7}$. (i) HAADF–STEM images of the areas marked in orange of (h). (j) IFFT image of (i) [61]. Copyright 2022, Wiley. (k) ACTEM image of MoS_2 monolayer with S-vacancies [62]. Copyright 2016, Springer Nature.
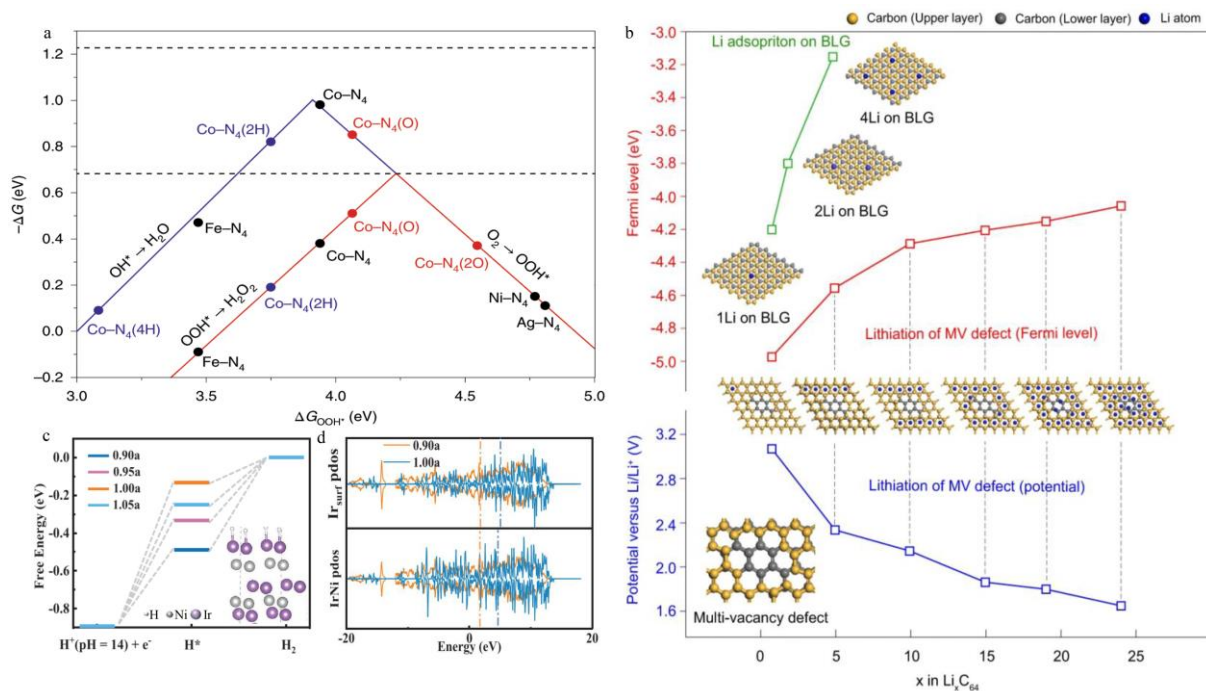
Fig. 4 (a) Catalytic active volcanoes producing H_2O (blue) and H_2O_2 (red) by ORR calculations [68]. Copyright 2020, Springer Nature. (b) Relaxed structures of lithiated BLG, MV, and fully lithiated MV (Li_3C_8), corresponding DFT calculations of the Fermi level, and redox potential of MV at different lithiation degrees [69]. Copyright 2021, Springer Nature. (c) The Gibbs free energies of DSIrNi for HER under various strains. (d) Comparison of PDOS profiles between 10%-strained and pristine structure [70]. Copyright 2020, Wiley.
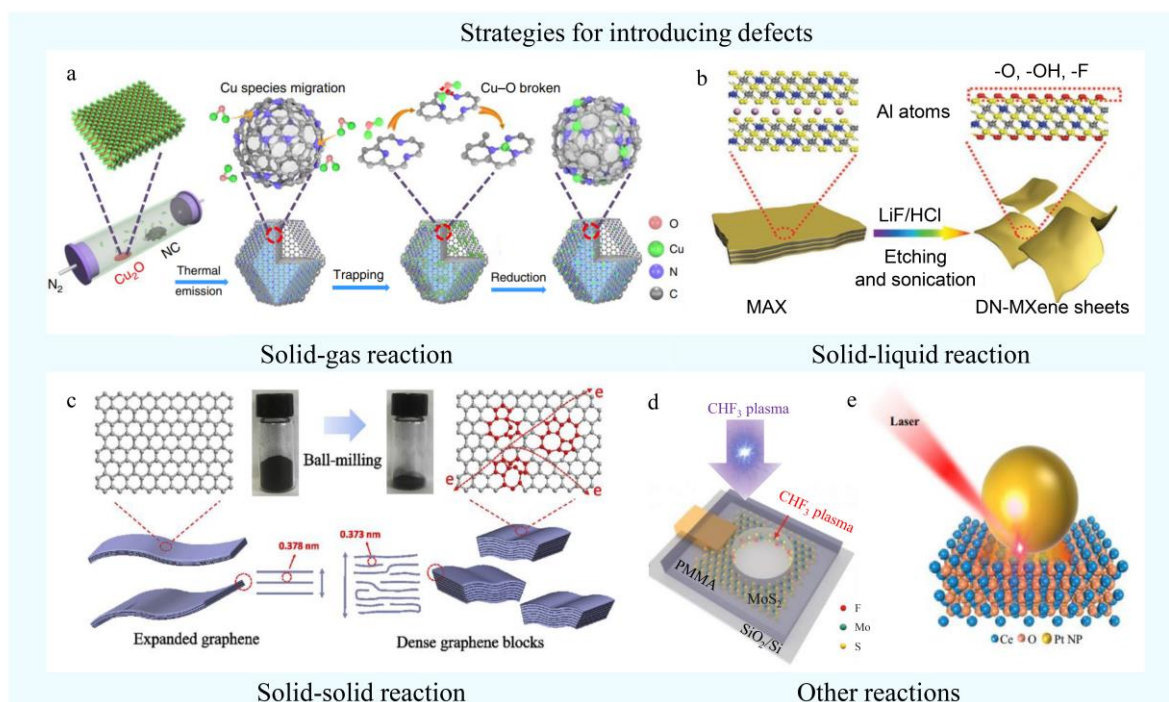
Fig. 5 (a) Schematic representation of Cu_2O vapor being trapped by N doped carbon to form Cu ISAS/N-C [74]. Copyright 2019, Springer Nature. (b) Schematic representation of tMAX etching into MXene with Ti vacancies in the liquid phase [79]. Copyright 2019, Wiley. (c) Diagram of the morphological and structural evolution process from expanded graphene to dense graphene bulks after ball milling [85]. Copyright 2020, Elsevier. (d) Schematic diagram of in-situ generation and doped etched edges of CHF_3 plasma on MoS_2 [91]. Copyright 2021, Wiley. (e) Diagram of the ultrafast laser-induced strong metal-support interactions in Pt/CeO_2 [98]. Copyright 2021, Springer Nature.
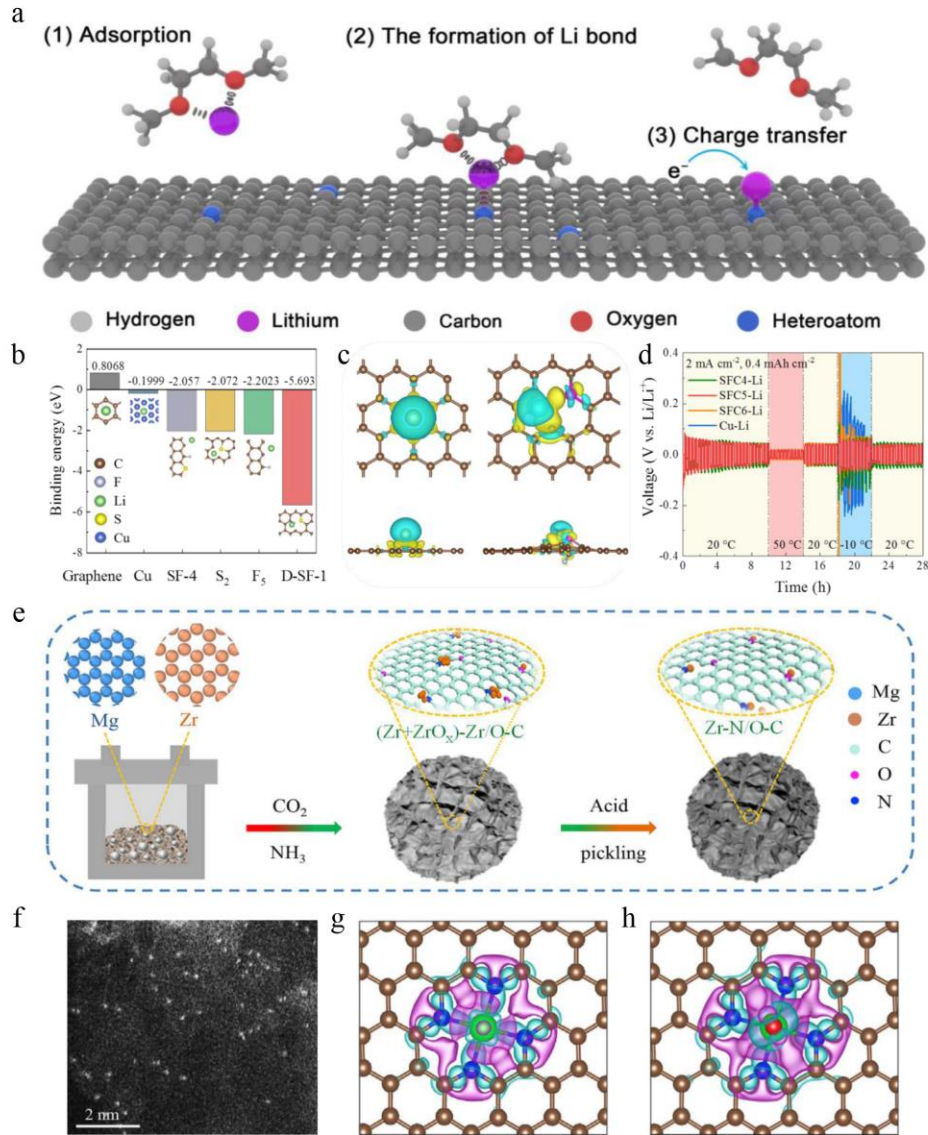
Fig. 6 (a) Schematic representation of the Li nucleation processes on conductive frameworks including absorption, Li bond formation, and charge transfer [100]. Copyright 2019, National Academy of Sciences. (b) Summary of calculated binding energies of Li with Cu, pure graphene, and different doping sites on SFC5. (c) The top view and the side view of the charge density differences of graphene, and D-SF-1 site with one Li atom adsorbed. (d) Cycling stability of symmetric cells that incorporated the different electrodes [53]. Copyright 2022, Elsevier. (e) Schematic representation of the synthesis procedure of atomic-dispersed Zr-N/O-C. (f) HAADF-STEM image of the Zr-N/O-C. g, h) Differential charge densities of ZrN4 (g) and ZrN4O (h) moieties, respectively [18]. Copyright 2022, Elsevier.
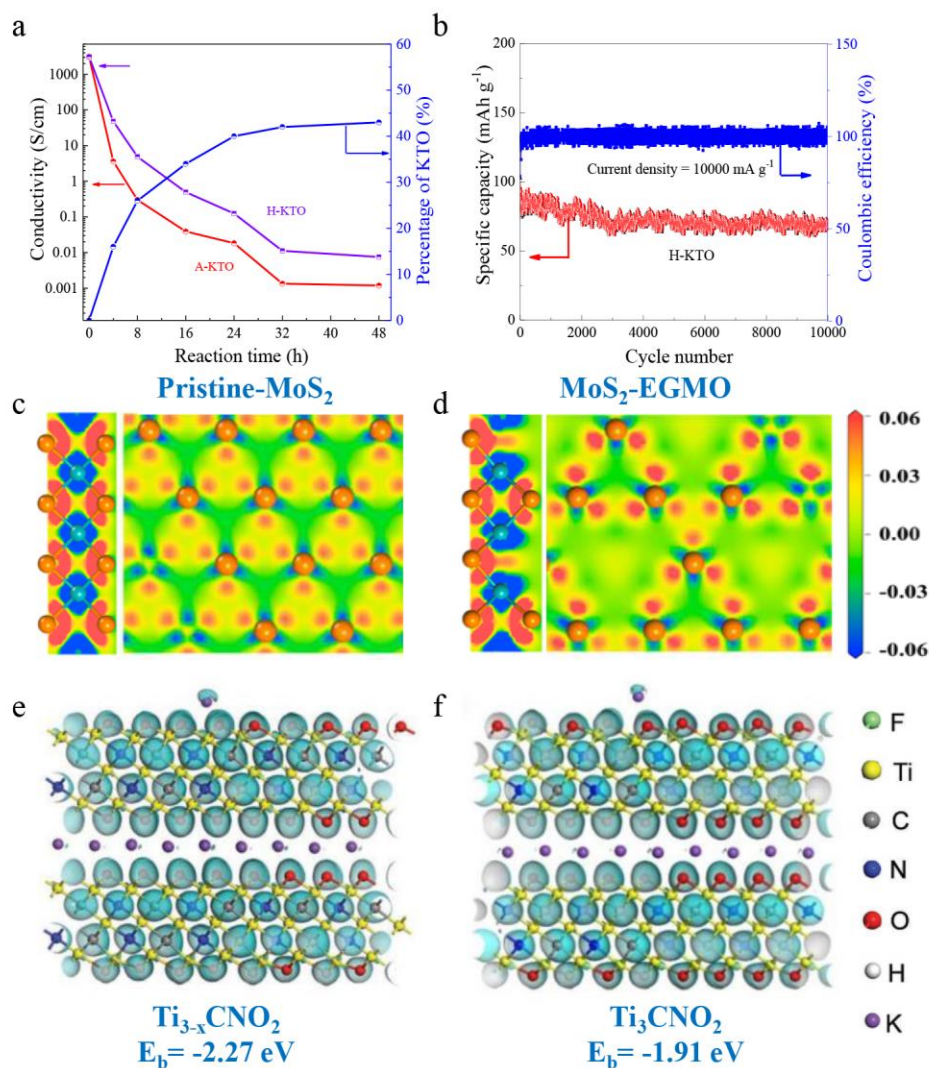
Fig. 7 (a) Effects of reaction time and hydrogenation treatment on the conductivity and KTO concentration of various samples. (b) Cycling properties of the H-KTO electrode at a current rate of 10 A g^{-1} [37]. Copyright 2017, Wiley. (c, d) Top-view and side view electron density difference maps of (c) P-MoS$_2$, and (d) MoS$_2$-EGMO [19]. Copyright 2020, American Chemical Society. (e, f) The deformation charge density of K atoms absorbed on Ti$_{3-x}$CNO$_2$ (e), and Ti$_3$CNO$_2$ (f) [79]. Copyright 2019, Wiley.
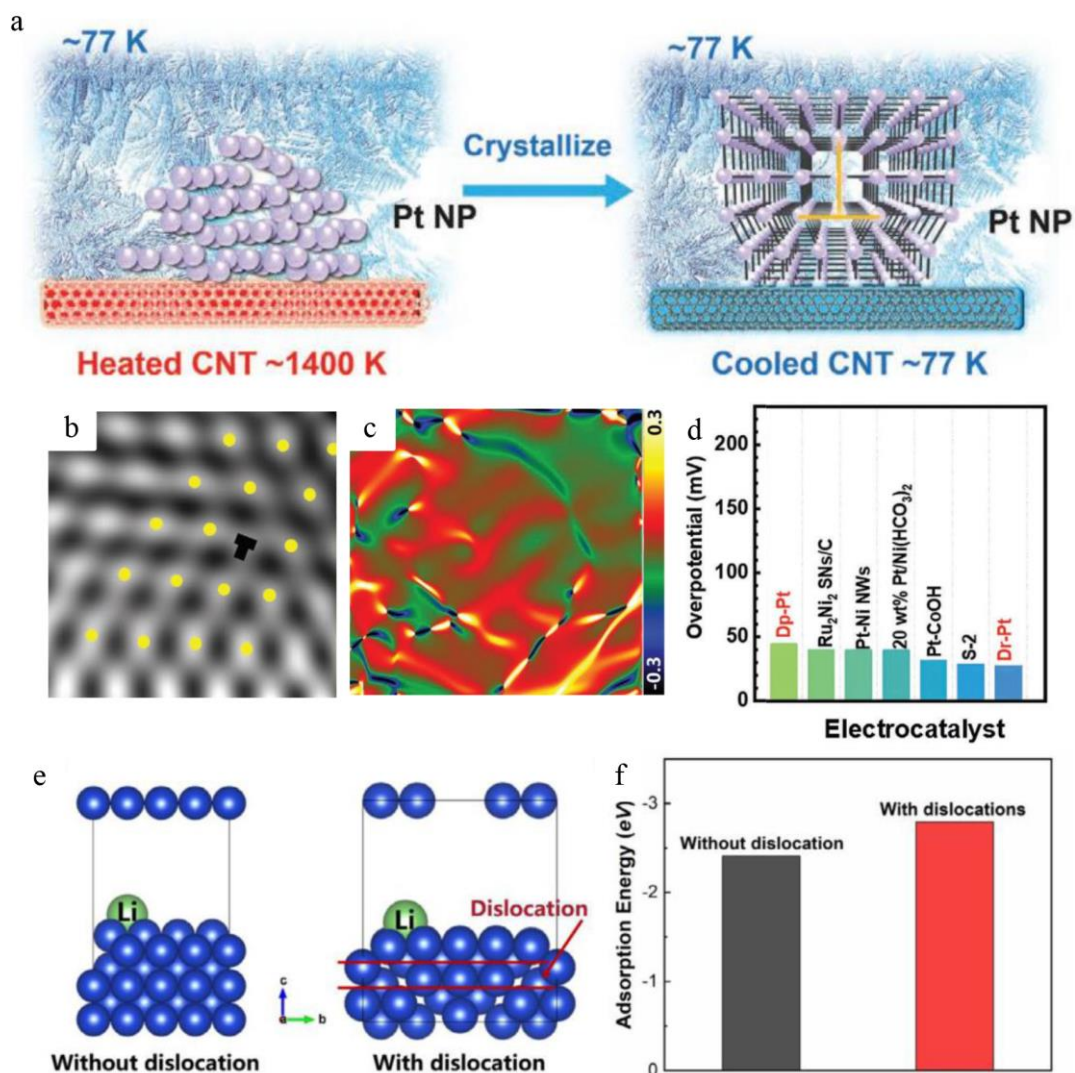
Fig. 8 (a) Schematic diagram of dislocation-rich platinum nanoparticles prepared by ambient HTS. **(b)** Filtered IFFT patterns of (011) planes of the Pt nanoparticle. **(c)** Strain distributions of e_{xx} and e_{yy}, which is related to the (011) planes. **(d)** Comparison of the overpotential of dislocation-rich dislocations in Pt with other state-of-the-art electrocatalysts at 10ma cm^{-2} [20]. Copyright 2021, Wiley. **(e, f)** DFT results and models for adsorption energy of copper foils with and without dislocations [102]. Copyright 2022, Elsevier.
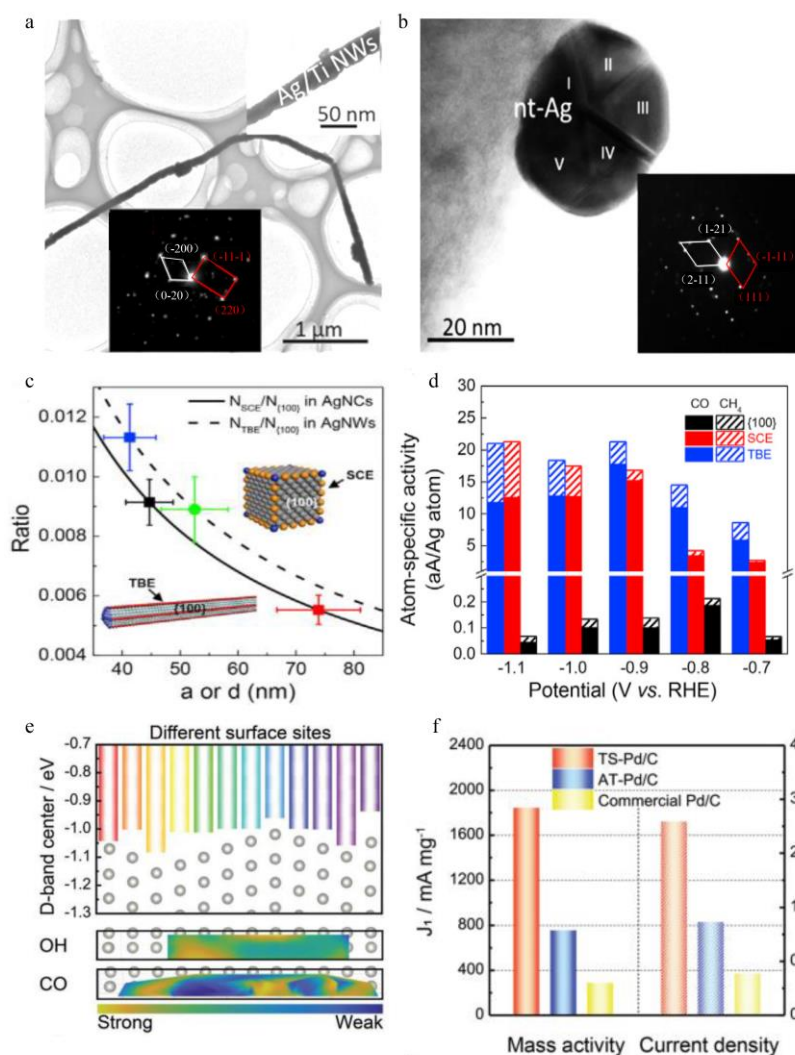
Fig. 9 (a) The high magnification TEM image and the SAED fringe of Ag/Ti nanowires. **(b)** The high magnification TEM image of nanoparticle with a five-fold twin [113]. Copyright 2016, American Chemical Society. **(c)** The ratio of atoms on SCEs (TBEs) and surface ($N_{(100)}$) in Ag NCs (NWs) as a function of the edge length (diameter). **(d)** Atom-specific activities for the formation of CO and CH_4 on single atom of the (100) surfaces, SCEs, and TBEs [114]. Copyright 2021, Elsevier. **(e)** Binding energy intensity distribution of d-band centers and CO and OH at different surface locations in defective Pd. **(f)** Histogram of mass activities and current densities of TS-Pd/C, AT-Pd/C, and commercial Pd/C [43]. Copyright 2022, Wiley.
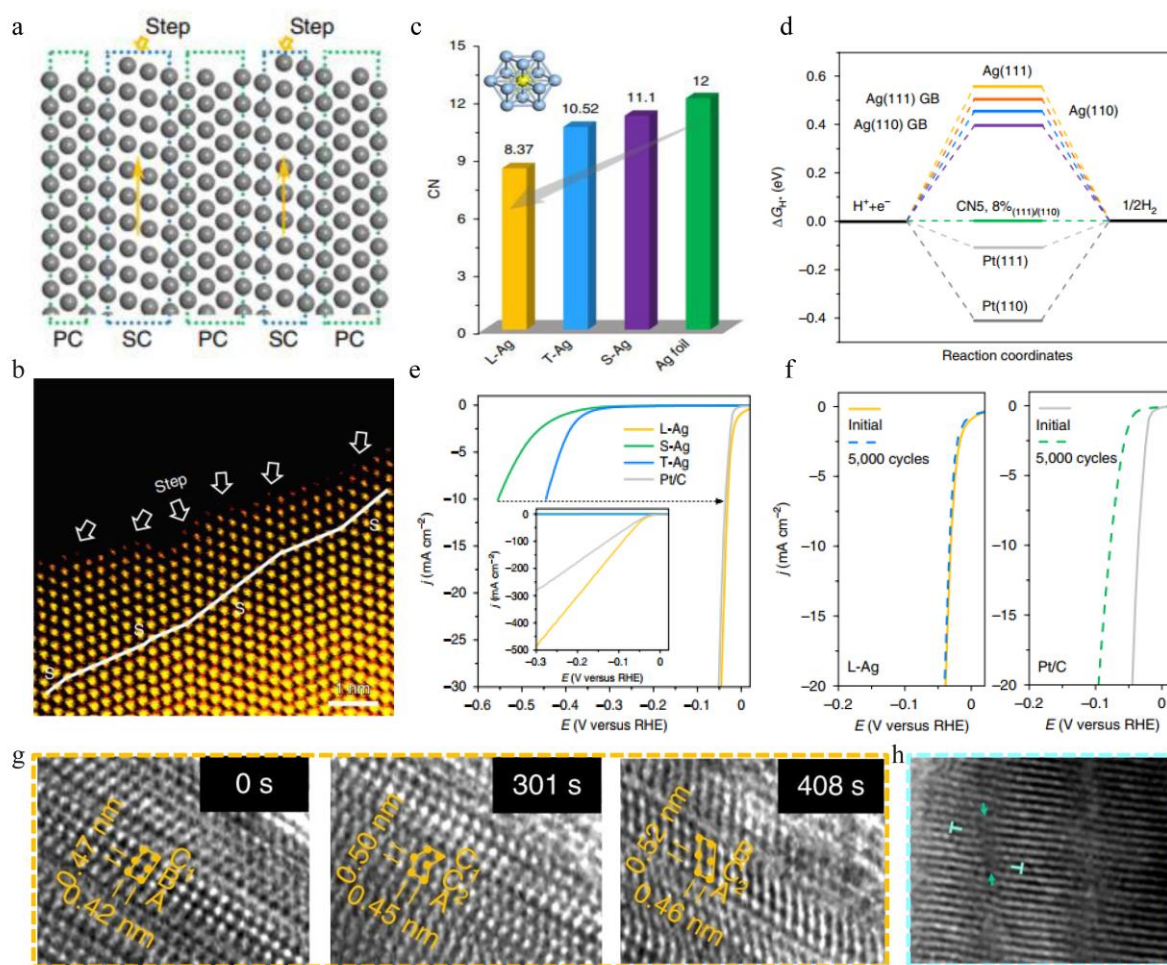
Fig. 10 (a, b) Illustration of stacking fault (a) and AC-HAADF-STEM image (b) of stacking faults in Ag nanocrystal. (c) The average coordination numbers of laser-generated Ag (L-Ag), monocrystal-Ag (S-Ag) and twin crystal-Ag (T-Ag). (d) ΔG_{H^*} comparison of the reaction coordinates of HER on different catalyst facets. (e) Polarization curves of L-Ag, S-Ag, T-Ag and Pt/C in 0.5 M H_2SO_4 with a scan rate of 5 mV s^{-1}, without insulation resistance compensation. (f) Polarization curves of L-Ag and Pt/C recorded before and after 5,000 CV cycles between 0 V and -0.1 V (*versus* RHE) [22]. Copyright 2019, Springer Nature. (g, h) Stacking fault (g) and dissociated dislocations (h) in Li_2MnO_3 during delithiation [117]. Copyright 2019, Springer Nature.
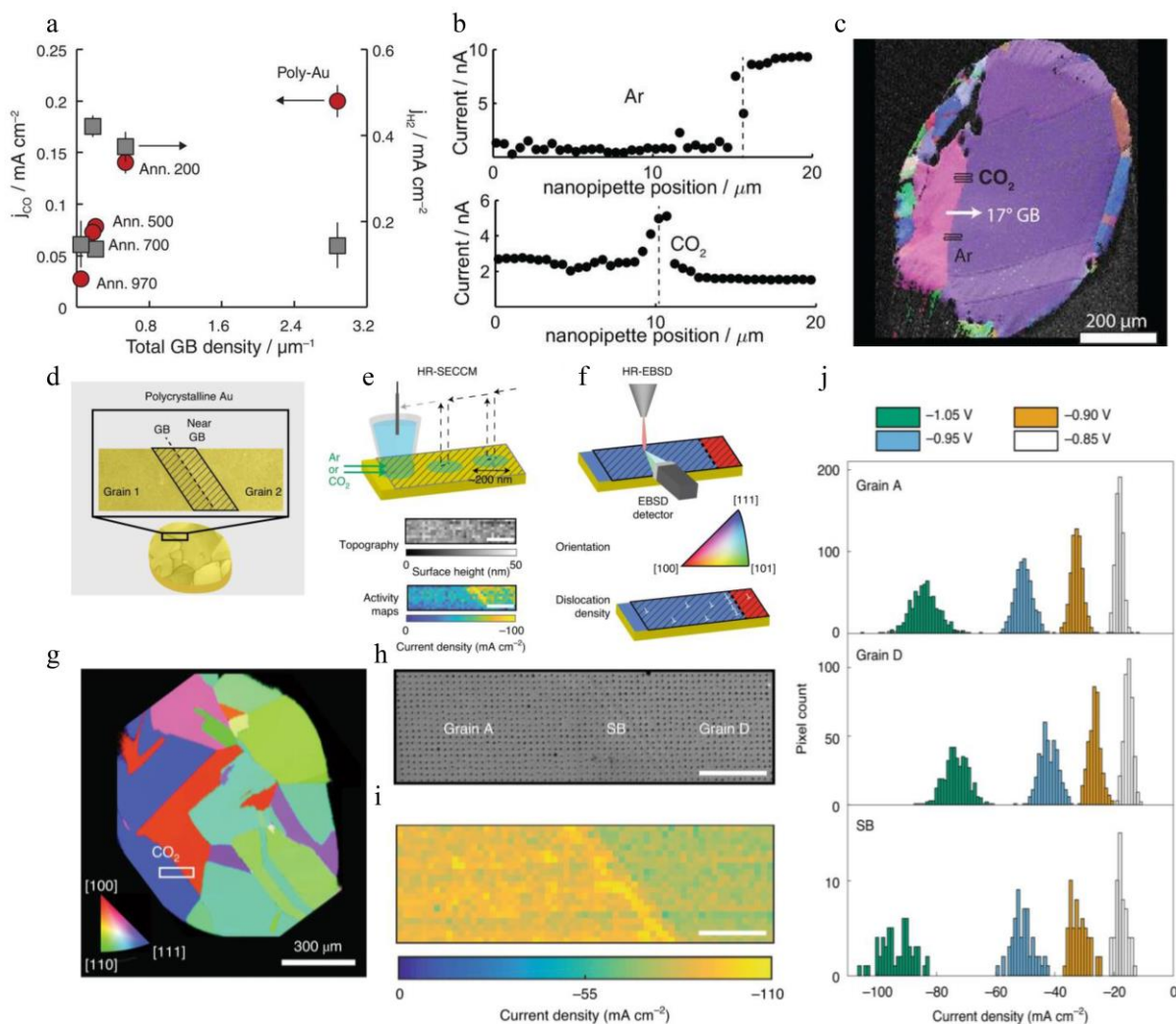
Fig. 11 (a, b) j_{CO} and j_{H2} *versus* total GB density for the five Au samples. b) Line scan generated from single constant potential electrolysis across the GB under 1 atm Ar. (c) EBSD orientation map of sample after annealing at 970 ℃ [72]. Copyright 2017, National Academy of Sciences. (d) A typical grain boundary structure probed by correlative SECCM and HR-EBSD measurements. (e) Illustration of voltammetric SECCM and (f) schematic of HR-EBSD grain mapping on polycrystalline Au surface. (g) EBSD directional plot of a typical polycrystalline Au sample along the z-direction. (h) SEM image of the region scanned with SECCM, showing residues left from droplet contact points. (i) The current density measured from SECCM at 1.05 V *versus* Ag/AgCl. (j) Histogram of current density for all pixels in the grains and grain boundaries regions. Copyright, 2021, Springer Nature [120].
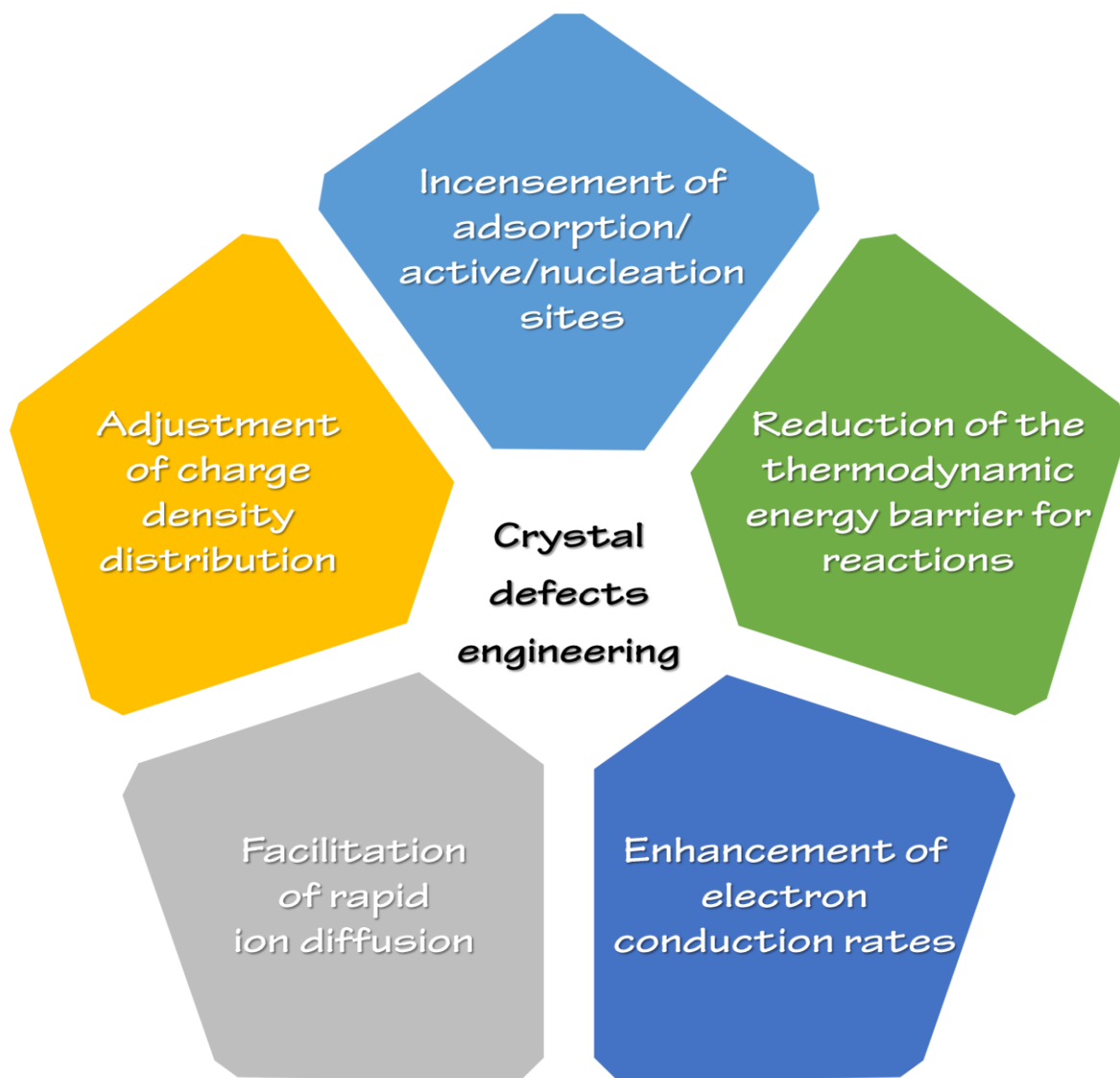
Fig. 12 Diagram of the relationship between defect type and electrochemical characteristics.
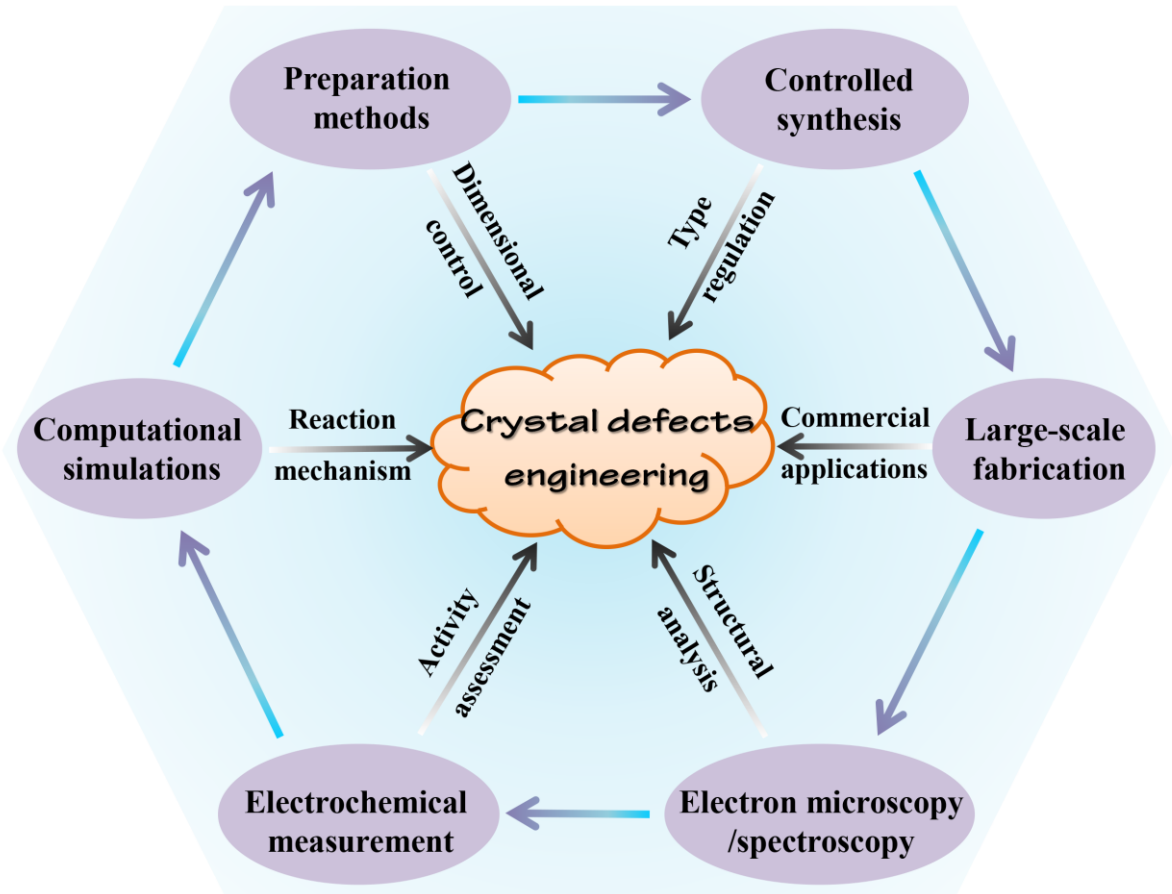
Fig. 13 Future development directions of the crystal defects engineering in the energy storage and conversion systems.

Table 1. Summary of techniques to characterize crystal defects in electrode materials.

Techniques	Identification	Advantages	Limitation	Ref.
EPR	Electron spin states with different *g* values correspond to various vacancy defects	One of the most direct and highly sensitive methods to observe paramagnetic substances; No complex processing of samples required	Unpaired electrons are all EPR active; Only paramagnetic samples can be tested	[48, 50, 143]
Raman	Peak shift, altered vibrational intensification, or appearance of new vibrational modes	High sensitivity, low sample concentration required	Susceptible to optical system parameters; Fluorescence interference; Low Raman signal strength	[52, 144]
XPS	Peak shift, intensity change or creation of new peaks	Suitable for a variety of materials, including insulation materials	Analysis of crystal defects limited to the surface of the material	[54, 145]
XAS	Valence states or bond length change	Available in a wide range of material sizes, including the single-atom level	Difficulty in distinguishing between dispersed atoms with small variations in atomic number	[59, 146]
XRD	Shifting peak positions and widening peak widths	No complex processing of samples required	Detecting defect concentrations is difficult due to low sensitivity	[147]
Microscopic imaging characterization techniques	Variation in interlayer spacing or atomic arrangement, atomic scale detection	Crystal defects types can be directly observed	The thickness must be thin enough to transmit electrons; Difficulties in sample preparation	[61, 62]

Table 2. Several typical manufacturing crystal defects strategies and their advantages and disadvantages.

Reaction types	Strategies	Advantages	Limitation	Ref.
Solid-gas reaction	Thermal treatment	High efficiency; Simple operation	High thermal energy consumption	[18, 74]
	Vapor deposition	Continuous and controllable large-area preparation	Low deposition rate	[75]
Solid-liquid reaction	Hydrothermal reaction	Short preparation time; Homogeneous distribution of defects in the material	Easily introduced -O/-OH functional groups	[37, 76]
	Acid etching			[79]
Solid-solid reaction	Ball milling	High efficiency; Simple operation; Easy for large-scale production; Wide range of applications	Cold welding effects; High energy consumption; Easily introduced solid impurities	[82, 86, 87]
Other reactions	Plasma-assisted etching	Distinctive species response characteristics; Adjustable operating requirements	Expensive equipment	[88, 90]
	Laser irradiation	Low thermal energy consumption; Selectivity; Rapid preparation		[92, 93, 148]

Table 3. Application of electrode material CDE reported in the literature in recent years in the field of batteries.

Battery type	Electrode	Defect category	Methods	Electrolyte	Potential window	Capacity	Ref.
Li ion battery	N-doped SnO_2	N doping	Other (Laser)	1M $LiPF_6$	0.01-3V	1195 mAh g^{-1} (1.4 A g^{-1}, 500 cycles)	[149]
Li ion battery	S/F doped carbon	S/F doping	Solid-gas (Thermal treatment)	1M $LiPF_6$	2.5-3.8V	107 mAh g^{-1} (0.1 A g^{-1}, 300 cycles)	[53]
Li ion battery	$Li_4Ti_5O_{12}$-TiO_2-C	Grain boundary	Solid-gas (Thermal treatment)	1M $LiPF_6$	1.0-2.5V	110 mAh g^{-1} (10 C, 100 cycles)	[119]
Li ion battery	Nanometric Si	Grain boundary	Solid-solid (Ball milling)	1M $LiPF_6$	0.01-1V	1600 mAh g^{-1} (0.48 A g^{-1}, 600 cycles)	[84]
Li ion battery	$LiMn_2O_4$	Twin	Solid-gas (Thermal treatment)	1M $LiPF_6$	3.4-4.5V	107 mAh g^{-1} (1 C, 500 cycles)	[42]
Li ion battery	Co_3O_4	Dislocation	Solid-gas (Thermal treatment)	1M $LiPF_6$	0.01-3V	1142 mAh g^{-1} (1 A g^{-1}, 200 cycles)	[40]
Li ion battery	MnO-Vo hexagonal sheets	O vacancies	Solid-gas (Thermal reduction)	1M $LiPF_6$	0.01-3V	825.2 mAh g^{-1} (1 A g^{-1}, 1000 cycles)	[35]
Li ion battery	SnS_2/SnO nanosheets	S vacancies	Other (Plasma)	1M $LiPF_6$	0.01-3V	998 mAh g^{-1} (200 mA g^{-1}, 200 cycyles)	[150]
Li ion battery	Bi_2MoO_6 sheets	O vacancies	Solid-liquid (Wet-chemical method)	1M $LiPF_6$	0.01-3V	478 mAh g^{-1} (2 A g^{-1}, 1500 cycles)	[151]
Li ion battery	TB-NMC442	Twin	Solid-gas (Thermal treatment)	1M $LiPF_6$	2.5-4.7V	124 mAh g^{-1}(1 C, 100 cycles)	[152]
Na ion battery	HMF-MoS_2	Mo vacancies	Solid-liquid (Acid etching)	1M $NaClO_4$	0.01-3V	384.3 mAh g^{-1} (100 mA g^{-1}, 100 cycles)	[32]
Na ion battery	Dense graphene blocks	O vacancies	Solid-solid (Ball milling)	1M $NaSO_3CF_3$	0.01-2.8 V	174 mAh g^{-1} (5 A g^{-1}, 3000 cycles)	[85]
Na ion battery	NC@MoS_2-VS	N doping and S vacancies	Solid-gas (Thermal reduction)	1M $NaClO_4$	0.001-3V	495 mAh g^{-1} (100 mA g^{-1}, 100 cycles)	[33]
Na ion battery	R-TiO_{2-x}-S	S doping	Other (Plasma)	1M $NaClO_4$	0.01-3V	265 mAh g^{-1} (50 mA g^{-1})	[153]
Na ion battery	N-doped 3D graphene	N doping	Other (Laser)	1M $NaClO_4$	0.005-2.5V	425 mAh g^{-1} (100	[154]

						mA g^{-1}, 200 cycles)	
Mg ion battery	B-TiO$_{2-x}$ nanoflakes	O vacancies	Solid-gas (Thermal oxidation)	0.4 M APC	0.05-2.1V	77 mAh g^{-1} (300 mA g^{-1}, 300 cycles)	[13]
K-ion battery	N-doped hollow carbon	N doping	Solid-gas (Thermal treatment)	0.8 M KPF$_6$	0.01-2.5V	161.3 mAh g^{-1} (1 A g^{-1}, 1600 cycles)	[155]
Zn ion battery	vanadium-defective V$_2$O$_3$	V vacancies	Solid-gas (Thermal treatment)	3 M Zn(CF$_3$SO$_3$)$_2$	0.1-1.3V	97 mAh g^{-1} (5 A g^{-1}, 30000 cycles)	[36]
Li-S battery	Ti$_{0.87}$O$_2$	Ti vacancies	Solid-gas (Thermal treatment)	1 M LiTFSI	1.7-2.8V	585 mAh g^{-1} (1 C, 5000 cycles)	[60]
Li-S battery	MoS$_{2-x}$/rGO/S	S vacancies	Solid-liquid (Liquid phase exfoliation)	1 M LiTFSI	1.7-2.8V	628.2 mAh g^{-1} (0.5 C, 600 cycles)	[156]

Table 4. Application of electrode material CDE reported in the literature in recent years in the field of electrocatalysis.

Catalytic type	Electrode	Detect category	Methods	Electrolyte	Performance	Stability	Ref.
HER	L-Ag NPs	Stacking faults	Other (Laser)	1M KOH	Overpotentials of 32 mV at 10 mA cm^{-2}	negligible decay after 2000 cycles	[22]
HER	2D CeO$_2$ nanosheets	Co doping and O vacancies	Solid-gas (Thermal treatment)	1M KOH	Overpotentials of 132 mV at 100 mA cm^{-2}	5% decay after 14 h at 150 mV	[157]
HER	Dr-Pt	Dislocation	Solid-gas (Thermal treatment)	1M KOH	Overpotentials of 26 mV at 10 mA cm^{-2}	negligible decay after 2000 cycles	[20]
HER	NiTiO$_3$/Ni	O vacancies	Solid-solid (Ball milling)	1M KOH	Overpotentials of 10 mV at 10 mA cm^{-2}	15 mV decay after 200 h at 100 mA cm^2	[34]
HER	2H-MoS$_2$	Grain boundary	Solid-gas (Thermal treatment)	0.5M H$_2$SO$_4$	Overpotentials of 136 mV at 10 mA cm^{-2}	negligible decay after 200 h at 10 mA cm^2	[105]
OER	L-Co$_3$O$_4$	O vacancies	Other (Laser)	1M KOH	Overpotentials of 270 mV at 10 mA cm^{-2}	4% decay after 30h at 10 mA cm^2	[31]
OER	CoFeLDHs-Ar	O, Co, and Fe vacancies	Other (Plasma)	1M KOH	Overpotentials of 266 mV at 10 mA cm^{-2} in OER	negligible decay after 2000 CV cycles	[158]
OER	N-Co$_9$S$_8$/G	N doping	Other (Plasma)	0.1M KOH	Overpotentials of 409 mV at 10 mA cm^{-2}	slightly positive shift after 2000 CV cycles	[159]
OER	NiCo/NLG-270	N doping	Other (Laser)	1M KOH	Overpotentials of 310 mV at 10 mA cm^{-2}	2% decay after 10 h at 10 mV	[160]
OER	(NiCo)$_3$Se$_4$ SABM	Ni and Co vacancies	Solid-solid (Ball milling)	1M KOH	Overpotentials of 268 mV at	4 mV overpotential	[81]

					10 mA cm^{-2}	increase after 100 h at 10 mA cm^2	
ORR	N,P-CGHNs	N and P doping	Solid-gas (Thermal treatment)	0.1M KOH	Half-wave potential of 0.82 V	negligible decay after 5000 CV cycles	[161]
ORR	Pd$_2$CoAg	Twin	Solid-liquid (Hydrothermal method)	0.1M KOH	Half-wave potential of 0.81 V	negligible decay after 5000 CV cycles	[78]
ORR	s-Zr-N-C	O, N, and Zr doping	Solid-solid (Ball milling)	0.1M KOH	Half-wave potential of 0.913 V	negligible decay after 10000 CV cycles	[18]
ORR	NSP-Gra	N, S, and P doping	Solid-solid (Ball milling)	0.1M KOH	Half-wave potential of 0.82 V	1 mA cm^{-2} decay after 5000 CV cycles	[82]
EOR	TS-Pd/C	Twin	Solid-gas (Thermal treatment)	1M KOH	Mass activity of 1846 mA mg^{-1}	~10% decay after 900 CV cycles	[43]

References

[1] S. Chu, A. Majumdar, Opportunities and challenges for a sustainable energy future, Nature 488 (2012) 294-303.

[2] L. Bu, N. Zhang, S. Guo, X. Zhang, J. Li, J. Yao, T. Wu, G. Lu, J.-Y. Ma, D. Su, Biaxially strained PtPb/Pt core/shell nanoplate boosts oxygen reduction catalysis, Science 354 (2016) 1410-1414.

[3] D. Larcher, J. Tarascon, Towards greener and more sustainable batteries for electrical energy storage, Nat. Chem. 7 (2015) 19-29.

[4] P. Poizot, F. Dolhem, Clean energy new deal for a sustainable world: from non-CO_2 generating energy sources to greener electrochemical storage devices, Energy Environ. Sci. 4 (2011) 2003-2019.

[5] C. Vivek, P. Ramkumar, P. Srividhya, M. Sivasubramanian, Recent strategies and trends in implanting of renewable energy sources for sustainability-A review, Mater.Today: Proceedings 46 (2021) 8204-8208.

[6] K. Divya, J. Østergaard, Battery energy storage technology for power systems-An overview, Electr. Power Syst. Res. 79 (2009) 511-520.

[7] Z. Shadike, E. Zhao, Y.N. Zhou, X. Yu, Y. Yang, E. Hu, S. Bak, L. Gu, X.Q. Yang, Advanced characterization techniques for sodium-ion battery studies, Adv. Energy Mater. 8 (2018) 1702588.

[8] Y. Ren, L. Zeng, H. Jiang, W. Ruan, Q. Chen, T. Zhao, Rational design of spontaneous reactions for protecting porous lithium electrodes in lithium-sulfur batteries, Nat. Commun. 10 (2019) 1-10.

[9] E. Marini, L. Jörissen, S. Brimaud, Rational design of a low-cost, durable and efficient bifunctional oxygen electrode for rechargeable metal-air batteries, J. Power Sources 482 (2021) 228900.

[10] T. Liu, L. Yu, J. Lu, T. Zhou, X. Huang, Z. Cai, A. Dai, J. Gim, Y. Ren, X. Xiao, Rational

design of mechanically robust Ni-rich cathode materials via concentration gradient strategy, Nat. Commun. 12 (2021) 1-10.

[11] J. Joo, T. Kim, J. Lee, S.I. Choi, K. Lee, Morphology‑controlled metal sulfides and phosphides for electrochemical water splitting, Adv. Mater. 31 (2019) 1806682.

[12] M.A.A.M. Abdah, N.H.N. Azman, S. Kulandaivalu, Y. Sulaiman, Review of the use of transition-metal-oxide and conducting polymer-based fibres for high-performance supercapacitors, Mater. Des. 186 (2020) 108199.

[13] M.H. Seo, M.G. Park, D.U. Lee, X. Wang, W. Ahn, S.H. Noh, S.M. Choi, Z.P. Cano, B. Han, Z. Chen, Bifunctionally active and durable hierarchically porous transition metal-based hybrid electrocatalyst for rechargeable metal-air batteries, Appl. Catal. B 239 (2018) 677-687.

[14] R. Mukherjee, A.V. Thomas, D. Datta, E. Singh, J. Li, O. Eksik, V.B. Shenoy, N. Koratkar, Defect-induced plating of lithium metal within porous graphene networks, Nat. Commun. 5 (2014) 3710.

[15] R.M. Lawrence, S.M. Unni, Defect induced nitrogen reduction reaction of carbon nanomaterials, Sustain. Energy Fuels 5 (2021) 3765-3790.

[16] K. Zhu, S. Wei, H. Shou, F. Shen, S. Chen, P. Zhang, C. Wang, Y. Cao, X. Guo, M. Luo, H. Zhang, B. Ye, X. Wu, L. He, L. Song, Defect engineering on V_2O_3 cathode for long-cycling aqueous zinc metal batteries, Nat. Commun. 12 (2021) 6878.

[17] Y. Zhou, Y. Chai, X. Li, Z. Wu, J. Lin, Y. Han, L. Li, H. Qi, Y. Gu, L. Kang, X. Wang, Defect-rich TiO_2 in situ evolved from MXene for the enhanced oxidative dehydrogenation of ethane to ethylene, ACS Catal. 11 (2021) 15223-15233.

[18] X. Zhao, J. Wang, J. Wang, M. Yang, C. Yan, G. Zou, S.T. John, C. Fernandez, Q. Peng, Atomically dispersed quintuple nitrogen and oxygen co-coordinated zirconium on graphene-type substrate for highly efficient oxygen reduction reaction, Cell Rep. Phy. Sci. 3 (2022) 100773.

[19] X. Wang, Y. Zhang, H. Si, Q. Zhang, J. Wu, L. Gao, X. Wei, Y. Sun, Q. Liao, Z. Zhang, K.

Ammarah, L. Gu, Z. Kang, Y. Zhang, Single-atom vacancy defect to trigger high-efficiency hydrogen evolution of MoS2, J. Am. Chem. Soc. 142 (2020) 4298-4308.

[20] S. Liu, Y. Shen, Y. Zhang, B. Cui, S. Xi, J. Zhang, L. Xu, S. Zhu, Y. Chen, Y. Deng, W. Hu, Extreme environmental thermal shock induced dislocation-rich Pt nanoparticles boosting hydrogen evolution reaction, Adv. Mater. 34 (2022) 2106973.

[21] A. Nie, L.Y. Gan, Y. Cheng, Q. Li, Y. Yuan, F. Mashayek, H. Wang, R. Klie, U. Schwingenschlogl, R. Shahbazian-Yassar, Twin boundary-assisted lithium ion transport, Nano Lett. 15 (2015) 610-615.

[22] Z. Li, J.-Y. Fu, Y. Feng, C.-K. Dong, H. Liu, X.-W. Du, A silver catalyst activated by stacking faults for the hydrogen evolution reaction, Nat. Catal. 2 (2019) 1107-1114.

[23] E. Zhu, W. Xue, S. Wang, X. Yan, J. Zhou, Y. Liu, J. Cai, E. Liu, Q. Jia, X. Duan, Y. Li, H. Heinz, Y. Huang, Enhancement of oxygen reduction reaction activity by grain boundaries in platinum nanostructures, Nano Res. 13 (2020) 3310-3314.

[24] R. Chattot, P. Bordet, I. Martens, J. Drnec, L. Dubau, F. Maillard, Building practical descriptors for defect engineering of electrocatalytic materials, ACS Catal. 10 (2020) 9046-9056.

[25] A.A. Saleh, N. Ahmed, A.H. Biby, N.K. Allam, Supercapattery electrode materials by Design: Plasma-induced defect engineering of bimetallic oxyphosphides for energy storage, J. Colloid Interface Sci. 603 (2021) 478-490.

[26] Y. Zhang, L. Tao, C. Xie, D. Wang, Y. Zou, R. Chen, Y. Wang, C. Jia, S. Wang, Defect engineering on electrode materials for rechargeable batteries, Adv. Mater. 32 (2020) 1905923.

[27] M. Liu, L. Jia, Z. Zhao, Y. Han, Y. Li, Q. Peng, Q. Zhang, Fast and robust lead (II) removal from water by bioinspired amyloid lysozyme fibrils conjugated with polyethyleneimine (PEI), Chem. Eng. J. 390 (2020) 124667.

[28] M. Wei, L. Huang, L. Li, F. Ai, J. Su, J. Wang, Coordinatively unsaturated PtCo flowers assembled with ultrathin nanosheets for enhanced oxygen reduction, ACS Catal. 12 (2022)

6478-6485.

[29] J.S. Park, S. Kim, Z. Xie, A. Walsh, Point defect engineering in thin-film solar cells, Nat. Rev. Mater. 3 (2018) 194-210.

[30] K.W. Böer, Handbook of the physics of thin-film solar cells, Springer Science & Business (2013).

[31] Z. Li, Y. Zhang, Y. Feng, C.Q. Cheng, K.W. Qiu, C.K. Dong, H. Liu, X.W. Du, Co_3O_4 nanoparticles with ultrasmall size and abundant oxygen vacancies for boosting oxygen involved reactions, Adv. Funct. Mater. 29 (2019) 1903444.

[32] Y. Li, R. Zhang, W. Zhou, X. Wu, H. Zhang, J. Zhang, Hierarchical MoS_2 hollow architectures with abundant Mo vacancies for efficient sodium storage, ACS Nano 13 (2019) 5533-5540.

[33] J. Liang, Z. Wei, C. Wang, J. Ma, Vacancy-induced sodium-ion storage in N-doped carbon Nanofiber@MoS_2 nanosheet arrays, Electrochim. Acta 285 (2018) 301-308.

[34] J. Cheng, P. Liu, T. Peng, Q. Liu, W. Chen, B. Liu, Y. Yuan, W. Zhang, F. Song, J. Gu, Mechanically alloyed $NiTiO_3$/transition metal heterostructures: introducing oxygen vacancies for exceptionally enhanced hydrogen evolution reaction activity, J. Mater. Chem. A 8 (2020) 14908-14914.

[35] Y. Zou, W. Zhang, N. Chen, S. Chen, W. Xu, R. Cai, C.L. Brown, D. Yang, X. Yao, Generating oxygen vacancies in MnO hexagonal sheets for ultralong life lithium storage with high capacity, ACS Nano 13 (2019) 2062-2071.

[36] K. Zhu, S. Wei, H. Shou, F. Shen, S. Chen, P. Zhang, C. Wang, Y. Cao, X. Guo, M. Luo, Defect engineering on V_2O_3 cathode for long-cycling aqueous zinc metal batteries, Nat. Commun. 12 (2021) 1-9.

[37] G. Zou, J. Guo, X. Liu, Q. Zhang, G. Huang, C. Fernandez, Q. Peng, Hydrogenated core-shell MAX@$K_2Ti_8O_{17}$ pseudocapacitance with ultrafast sodium storage and long-term cycling, Adv. Energy Mater. 7 (2017) 1700700.

[38] S. Eswarappa Prameela, P. Yi, M.L. Falk, T.P. Weihs, Strategic control of atomic-scale defects for tuning properties in metals, Nat. Rev. Phy. 3 (2021) 148-149.

[39] R.P. Patil, D. Doan, Z.H. Aitken, S. Chen, M.T. Kiani, C.M. Barr, K. Hattar, Y.-W. Zhang, X.W. Gu, Hardening in Au-Ag nanoboxes from stacking fault-dislocation interactions, Nat. Commun. 11 (2020) 1-9.

[40] C. Yan, G. Chen, J. Sun, C. Lv, J. Pei, Edge dislocation surface modification: A new and efficient strategy for realizing outstanding lithium storage performance, Nano Energy 15 (2015) 558-566.

[41] Z. Qiao, L. Lin, X. Yan, W. Guo, Q. Chen, Q. Xie, X. Han, J. Lin, L. Wang, D.L. Peng, Function and application of defect chemistry in high-capacity electrode materials for Li-based batteries, Chem. Asian J. 15 (2020) 3620-3636.

[42] R. Wang, X. Chen, Z. Huang, J. Yang, F. Liu, M. Chu, T. Liu, C. Wang, W. Zhu, S. Li, S. Li, J. Zheng, J. Chen, L. He, L. Jin, F. Pan, Y. Xiao, Twin boundary defect engineering improves lithium-ion diffusion for fast-charging spinel cathode materials, Nat. Commun. 12 (2021) 3085.

[43] C. Liu, Y. Shen, J. Zhang, G. Li, X. Zheng, X. Han, L. Xu, S. Zhu, Y. Chen, Y. Deng, W. Hu, Multiple twin boundary-regulated metastable Pd for ethanol oxidation reaction, Adv. Energy Mater. 12 (2022) 2103505.

[44] U. Dahmen, Phase transformations, crystallographic aspects, Encycl. Phy. Sci. Technol. 10 (1986) 319-354.

[45] N. Browning, M. Chisholm, S. Pennycook, D. Norton, D.J.P.C.S. Lowndes, Correlation between hole depletion and atomic structure at high angle grain boundaries in $YBa_2Cu_3O_{7-\delta}$, Physica C: Superconductivity 212 (1993) 185-190.

[46] D. Brandon, The structure of high-angle grain boundaries, Acta metall. 14 (1966) 1479-1484.

[47] B. Wang, W. Zhang, G. Liu, H. Chen, Y.X. Weng, H. Li, P.K. Chu, J. Xia, Excited

electron-rich $Bi^{(3-x)+}$ sites: A quantum well-like structure for highly promoted selective photocatalytic CO_2 reduction performance, Adv. Funct. Mater. 32 (2022) 2202885.

[48] Z. Wang, R. Lin, Y. Huo, H. Li, L. Wang, Formation, detection, and function of oxygen vacancy in metal oxides for solar energy conversion, Adv. Funct. Mater. 32 (2022) 2109503.

[49] Z. Tian, C. Han, Y. Zhao, W. Dai, X. Lian, Y. Wang, Y. Zheng, Y. Shi, X. Pan, Z. Huang, Efficient photocatalytic hydrogen peroxide generation coupled with selective benzylamine oxidation over defective ZrS_3 nanobelts, Nat. Commun. 12 (2021) 1-10.

[50] S. Liao, B. Pan, H. Li, D. Zhang, B. Xing, Detecting free radicals in biochars and determining their ability to inhibit the germination and growth of corn, wheat and rice seedlings, Environ. Sci. Technol. 48 (2014) 8581-8587.

[51] L.G. Cançado, A. Jorio, E.M. Ferreira, F. Stavale, C.A. Achete, R.B. Capaz, M.V.d.O. Moutinho, A. Lombardo, T. Kulmala, A.C. Ferrari, Quantifying defects in graphene via Raman spectroscopy at different excitation energies, Nano Lett. 11 (2011) 3190-3196.

[52] A.C. Ferrari, D.M. Basko, Raman spectroscopy as a versatile tool for studying the properties of graphene, Nat. Nanotechnol. 8 (2013) 235-246.

[53] J. Wang, M. Yang, J. Wang, D. Liu, G. Zou, B. Liu, S.T. John, L. Li, L. Ren, Q. Peng, Lithiation MAX derivative electrodes with low overpotential and long-term cyclability in a wide-temperature range, Energy Stor. Mater. 47 (2022) 611-619.

[54] K. Murugappan, E.M. Anderson, D. Teschner, T.E. Jones, K. Skorupska, Y. Román-Leshkov, Operando NAP-XPS unveils differences in MoO_3 and Mo_2C during hydrodeoxygenation, Nat. Catal. 1 (2018) 960-967.

[55] J. Xu, G. Shao, X. Tang, F. Lv, H. Xiang, C. Jing, S. Liu, S. Dai, Y. Li, J. Luo, Z. Zhou, Frenkel-defected monolayer MoS_2 catalysts for efficient hydrogen evolution, Nat. Commun. 13 (2022) 1-8.

[56] G. Greczynski, L. Hultman, Compromising science by ignorant instrument calibration-need to revisit half a century of published XPS data, Angew. Chem. Int. Ed. 59

(2020) 5002-5006.

[57] G. Greczynski, L. Hultman, The same chemical state of carbon gives rise to two peaks in X-ray photoelectron spectroscopy, Sci. Rep. 11 (2021) 1-5.

[58] W. Lu, L. Yan, W. Ye, J. Ning, Y. Zhong, Y. Hu, Defect engineering of electrode materials towards superior reaction kinetics for high-performance supercapacitors, J. Mater. Chem. A 10 (2022) 15267–15296.

[59] J. Yano, V.K. Yachandra, X-ray absorption spectroscopy, Photosyn. Res. 102 (2009) 241-254.

[60] P. Xiong, F. Zhang, X. Zhang, Y. Liu, Y. Wu, S. Wang, J. Safaei, B. Sun, R. Ma, Z. Liu, Atomic-scale regulation of anionic and cationic migration in alkali metal batteries, Nat. Commun. 12 (2021) 1-15.

[61] Y. Han, X. Feng, B. Gan, J. He, J. Feng, M. Zhao, Z. Li, Z. Zou, Manipulation of sulfur vacancies and dislocations in $Mn_{0.3}Cd_{0.7}S$ nanorods with modification of Co_2P toward photocatalytic H_2 evolution, Sol. RRL 6 (2022) 2200516.

[62] H. Li, C. Tsai, A.L. Koh, L. Cai, A.W. Contryman, A.H. Fragapane, J. Zhao, H.S. Han, H.C. Manoharan, F. Abild-Pedersen, Activating and optimizing MoS_2 basal planes for hydrogen evolution through the formation of strained sulphur vacancies, Nat. Mater. 15 (2016) 48-53.

[63] H.-S. Kim, J.B. Cook, H. Lin, J.S. Ko, S.H. Tolbert, V. Ozolins, B. Dunn, Oxygen vacancies enhance pseudocapacitive charge storage properties of MoO_{3-x}, Nat. Mater. 16 (2017) 454-460.

[64] Y. Yin, Y. Zhang, T. Gao, T. Yao, X. Zhang, J. Han, X. Wang, Z. Zhang, P. Xu, P. Zhang, Synergistic phase and disorder engineering in $1T-MoSe_2$ nanosheets for enhanced hydrogen-evolution reaction, Adv. Mater. 29 (2017) 1700311.

[65] S. Kang, J.-J. Koo, H. Seo, Q.T. Truong, J.B. Park, S.C. Park, Y. Jung, S.-P. Cho, K.T. Nam, Z.H. Kim, Defect-engineered MoS_2 with extended photoluminescence lifetime for

high-performance hydrogen evolution, J. Mater. Chem. C 7 (2019) 10173-10178.

[66] Y.-C. Lin, P.-Y. Teng, C.-H. Yeh, M. Koshino, P.-W. Chiu, K. Suenaga, Structural and chemical dynamics of pyridinic-nitrogen defects in graphene, Nano Lett. 15 (2015) 7408-7413.

[67] B. Hammer, J.K. Nørskov, Theoretical surface science and catalysis-calculations and concepts, Adv. Catal. 45 (2000) 71-129.

[68] E. Jung, H. Shin, B.-H. Lee, V. Efremov, S. Lee, H.S. Lee, J. Kim, W. Hooch Antink, S. Park, K.-S. Lee, Atomic-level tuning of Co-N-C catalyst for high-performance electrochemical H_2O_2 production, Nat. Mater. 19 (2020) 436-442.

[69] H. Kwon, J.-H. Lee, Y. Roh, J. Baek, D.J. Shin, J.K. Yoon, H.J. Ha, J.Y. Kim, H.-T. Kim, An electron-deficient carbon current collector for anode-free Li-metal batteries, Nat. Commun. 12 (2021) 1-13.

[70] S. Liu, Z. Hu, Y. Wu, J. Zhang, Y. Zhang, B. Cui, C. Liu, S. Hu, N. Zhao, X. Han, A. Cao, Y. Chen, Y. Deng, W. Hu, Dislocation-strained IrNi alloy nanoparticles driven by thermal shock for the hydrogen evolution reaction, Adv. Mater. 32 (2020) 2006034.

[71] P. Li, Z. Jiang, X. Huang, X. Lu, J. Xie, S. Cheng, Nitrofullerene as an electrolyte-compatible additive for high-performance sodium metal batteries, Nano Energy 89 (2021) 106396.

[72] R.G. Mariano, K. McKelvey, H.S. White, M.W. Kanan, Selective increase in CO_2 electroreduction activity at grain-boundary surface terminations, Science 358 (2017) 1187-1192.

[73] C. Chu, N. Wang, L. Li, L. Lin, F. Tian, Y. Li, J. Yang, S.-x. Dou, Y. Qian, Uniform nucleation of sodium in 3D carbon nanotube framework via oxygen doping for long-life and efficient Na metal anodes, Energy Stor. Mater. 23 (2019) 137-143.

[74] Z. Yang, B. Chen, W. Chen, Y. Qu, F. Zhou, C. Zhao, Q. Xu, Q. Zhang, X. Duan, Y. Wu, Directly transforming copper (I) oxide bulk into isolated single-atom copper sites catalyst

through gas-transport approach, Nat. Commun. 10 (2019) 1-7.

[75] X. Li, J. Zhou, J. Zhang, M. Li, X. Bi, T. Liu, T. He, J. Cheng, F. Zhang, Y. Li, Bamboo-like nitrogen-doped carbon nanotube forests as durable metal-free catalysts for self-powered flexible Li-CO$_2$ batteries, Adv. Mater. 31 (2019) 1903852.

[76] B. Ge, Y. Sun, J. Guo, X. Yan, C. Fernandez, Q. Peng, A Co-doped MnO$_2$ catalyst for Li-CO$_2$ batteries with low overpotential and ultrahigh cyclability, Small 15 (2019) 1902220.

[77] Y. Wu, K. Yue, Y. Wang, C. Chen, W. Lü, L. Duan, Controlled synthesis of MnOOH multilayer nanowires as anode materials for lithium-ion batteries, Mater. Charact. 118 (2016) 405-410.

[78] S. Liu, H. Zhang, X. Mu, C. Chen, Surface reconstruction engineering of twinned Pd$_2$CoAg nanocrystals by atomic vacancy inducement for hydrogen evolution and oxygen reduction reactions, Appl. Catal. B 241 (2019) 424-429.

[79] X. Tang, D. Zhou, P. Li, X. Guo, B. Sun, H. Liu, K. Yan, Y. Gogotsi, G. Wang, MXene-based dendrite-free potassium metal batteries, Adv. Mater. 32 (2020) 1906739.

[80] M. Kumar, X. Xiong, Z. Wan, Y. Sun, D.C.W. Tsang, J. Gupta, B. Gao, X. Cao, J. Tang, Y.S. Ok, Ball milling as a mechanochemical technology for fabrication of novel biochar nanomaterials, Bioresour. Technol. 312 (2020) 123613.

[81] J. Abed, S. Ahmadi, L. Laverdure, A. Abdellah, C.P. O'Brien, K. Cole, P. Sobrinho, D. Sinton, D. Higgins, N.J. Mosey, S.J. Thorpe, E.H. Sargent, In situ formation of nano Ni-Co oxyhydroxide enables water oxidation electrocatalysts durable at high current densities, Adv. Mater. 33 (2021) 2103812.

[82] Y. Wang, N. Xu, R. He, L. Peng, D. Cai, J. Qiao, Large-scale defect-engineering tailored tri-doped graphene as a metal-free bifunctional catalyst for superior electrocatalytic oxygen reaction in rechargeable Zn-air battery, Appl. Catal. B 285 (2021) 119811.

[83] J.E. Muñoz, J. Cervantes, R. Esparza, G. Rosas, Iron nanoparticles produced by high-energy ball milling, J. Nanopart. Res. 9 (2007) 945-950.

[84] M. Gauthier, D. Mazouzi, D. Reyter, B. Lestriez, P. Moreau, D. Guyomard, L. Roué, A low-cost and high performance ball-milled Si-based negative electrode for high-energy Li-ion batteries, Energy Environ. Sci. 6 (2013) 2145-2155.

[85] Y. Dong, X. Lin, D. Wang, R. Yuan, S. Zhang, X. Chen, L.G. Busheva, A.V. Okotrub, H. Song, Modulating the defects of graphene blocks by ball-milling for ultrahigh gravimetric and volumetric performance and fast sodium storage, Energy Stor. Mater. 30 (2020) 287-295.

[86] G.-F. Han, F. Li, A.I. Rykov, Y.-K. Im, S.-Y. Yu, J.-P. Jeon, S.-J. Kim, W. Zhou, R. Ge, Z. Ao, Abrading bulk metal into single atoms, Nat. Nanotechnol. 17 (2022) 403-407.

[87] A. Restrepo, J. Ríos, F. Arango, E. Correa, A. Zuleta, A. Valencia-Escobar, F. Bolivar, J. Castaño, F. Echeverría, Characterization of titanium powders processed in n-hexane by high-energy ball milling, Int. J. Adv. Manuf. Technol. 110 (2020) 1681-1690.

[88] H. Liang, A.N. Gandi, D.H. Anjum, X. Wang, U. Schwingenschlogl, H.N. Alshareef, Plasma-assisted synthesis of NiCoP for efficient overall water splitting, Nano Lett. 16 (2016) 7718-7725.

[89] H. Liang, F. Ming, H.N. Alshareef, Applications of plasma in energy conversion and storage materials, Adv. Energy Mater. 8 (2018) 1801804.

[90] S. Li, Z. Lu, B. Yuan, R. Hu, M. Zhu, Applications of plasma-assisted systems for advanced electrode material synthesis and modification, ACS Appl. Mater. Interfaces 13 (2021) 13909-13919.

[91] R. Zhang, M. Zhang, H. Yang, G. Li, S. Xing, M. Li, Y. Xu, Q. Zhang, S. Hu, H. Liao, Creating fluorine-doped MoS_2 edge electrodes with enhanced hydrogen evolution activity, Small Methods 5 (2021) 2100612.

[92] B.H. Seo, J. Youn, M. Shim, Direct laser writing of air-stable p-n junctions in graphene, ACS Nano 8 (2014) 8831-8836.

[93] R.C. Forsythe, C.P. Cox, M.K. Wilsey, A.M. Muller, Pulsed laser in liquids made nanomaterials for catalysis, Chem. Rev. 121 (2021) 7568-7637.

[94] Y. Jia, L. Zhang, A. Du, G. Gao, J. Chen, X. Yan, C.L. Brown, X. Yao, Defect graphene as a trifunctional catalyst for electrochemical reactions, Adv. Mater. 28 (2016) 9532-9538.

[95] W. Wang, L. Shang, G. Chang, C. Yan, R. Shi, Y. Zhao, G.I. Waterhouse, D. Yang, T. Zhang, Intrinsic carbon-defect-driven electrocatalytic reduction of carbon dioxide, Adv. Mater. 31 (2019) 1808276.

[96] M. Yu, F. Waag, C.K. Chan, C. Weidenthaler, S. Barcikowski, H. Tüysüz, Laser fragmentation-induced defect-rich cobalt oxide nanoparticles for electrochemical oxygen evolution reaction, ChemSusChem 13 (2020) 520-528.

[97] Y. Qin, Q. Li, J. Xu, X. Wang, G. Zhao, C. Liu, X. Yan, Y. Long, S. Yan, S. Li, CoO-Co nanocomposite anode with enhanced electrochemical performance for lithium-ion batteries, Electrochim. Acta 224 (2017) 90-95.

[98] J. Zhang, D. Zhu, J. Yan, C.A. Wang, Strong metal-support interactions induced by an ultrafast laser, Nat. Commun. 12 (2021) 6665.

[99] R. Paul, F. Du, L. Dai, Y. Ding, Z.L. Wang, F. Wei, A. Roy, 3D heteroatom-doped carbon nanomaterials as multifunctional metal-free catalysts for integrated energy devices, Adv. Mater. 31 (2019) 1805598.

[100] X. Chen, X.-R. Chen, T.-Z. Hou, B.-Q. Li, X.-B. Cheng, R. Zhang, Q. Zhang, Lithiophilicity chemistry of heteroatom-doped carbon to guide uniform lithium nucleation in lithium metal anodes, Sci. Adv. 5 (2019) eaau7728.

[101] A. Kumar, X. Liu, J. Lee, B. Debnath, A.R. Jadhav, X. Shao, V.Q. Bui, Y. Hwang, Y. Liu, M.G. Kim, Discovering ultrahigh loading of single-metal-atoms via surface tensile-strain for unprecedented urea electrolysis, Energy Environ. Sci. 14 (2021) 6494-6505.

[102] L. Qin, Y. Wu, M. Shen, B. Song, Y. Li, S. Sun, H. Zhang, C. Liu, J. Chen, Straining copper foils to regulate the nucleation of lithium for stable lithium metal anode, Energy Stor. Mater. 44 (2022) 278-284.

[103] J.Y. Huang, L. Zhong, C.M. Wang, J.P. Sullivan, W. Xu, L.Q. Zhang, S.X. Mao, N.S.

Hudak, X.H. Liu, A. Subramanian, In situ observation of the electrochemical lithiation of a single SnO_2 nanowire electrode, Science 330 (2010) 1515-1520.

[104] L. Beaulieu, K. Eberman, R. Turner, L. Krause, J. Dahn, Colossal reversible volume changes in lithium alloys, ECS Solid State Lett. 4 (2001) A137.

[105] J. Zhu, Z.-C. Wang, H. Dai, Q. Wang, R. Yang, H. Yu, M. Liao, J. Zhang, W. Chen, Z. Wei, Boundary activated hydrogen evolution reaction on monolayer MoS_2, Nat. Commun. 10 (2019) 1-7.

[106] L. Beaulieu, K. Eberman, R. Turner, L. Krause, J. Dahn, Colossal reversible volume changes in lithium alloys, Electrochem. Solid State Lett. 4 (2001) A137.

[107] L. Beaulieu, T. Hatchard, A. Bonakdarpour, M. Fleischauer, J. Dahn, Reaction of Li with alloy thin films studied by in situ AFM, J. Electrochem. Soc. 150 (2003) A1457.

[108] A. Singer, M. Zhang, S. Hy, D. Cela, C. Fang, T. Wynn, B. Qiu, Y. Xia, Z. Liu, A. Ulvestad, J.W. N. Hua, H. Liu, M. Sprung, A. V. Zozulya, E. Maxey, R. Harder, Y. S. Meng , O. G. Shpyrko, Nucleation of dislocations and their dynamics in layered oxide cathode materials during battery charging, Nat. Energy 3 (2018) 641-647.

[109] B. Ge, M. Yang, Q. Zu, J. Guo, Y. Tian, Q. Peng, Lithium cluster segregation in coherent contraction twin boundaries of magnesium alloys, Acta Mater. 201 (2020) 477-487.

[110] Q. Peng, Y. Sun, J. Wang, Q. Zu, M. Yang, H. Fu, Structural characteristics of {101-1} contraction twin-twin interaction in magnesium, Acta Mater. 192 (2020) 60-66.

[111] P. Sathiyamoorthi, H.S. Kim, High-entropy alloys with heterogeneous microstructure: Processing and mechanical properties, Prog. Mater. Sci. 123 (2022) 100709.

[112] C. Tang, P. Gong, T. Xiao, Z. Sun, Direct electrosynthesis of 52% concentrated CO on silver's twin boundary, Nat. Commun. 12 (2021) 2139.

[113] Z. Zhang, H. Li, G. Zou, C. Fernandez, B. Liu, Q. Zhang, J. Hu, Q. Peng, Self-reduction synthesis of new MXene/Ag composites with unexpected electrocatalytic activity, ACS Sustain. Chem. Eng. 4 (2016) 6763-6771.

[114] F. Hu, S.C. Abeyweera, J. Yu, D. Zhang, Y. Wang, Q. Yan, Y. Sun, Quantifying electrocatalytic reduction of CO_2 on twin boundaries, Chem 6 (2020) 3007-3021.

[115] H. Xie, T. Wang, J. Liang, Q. Li, S. Sun, Cu-based nanocatalysts for electrochemical reduction of CO_2, Nano Today 21 (2018) 41-54.

[116] S. Zhou, M. Zhao, T.-H. Yang, Y. Xia, Decahedral nanocrystals of noble metals: Synthesis, characterization, and applications, Mater. Today 22 (2019) 108-131.

[117] Q. Li, Z. Yao, E. Lee, Y. Xu, M.M. Thackeray, C. Wolverton, V.P. Dravid, J. Wu, Dynamic imaging of crystalline defects in lithium-manganese oxide electrodes during electrochemical activation to high voltage, Nat. Commun. 10 (2019) 1692.

[118] M. Han, Z. Liu, X. Shen, L. Yang, X. Shen, Q. Zhang, X. Liu, J. Wang, H.J. Lin, C.T. Chen, C.W. Pao, J.L. Chen, Q. Kong, X. Yu, R. Yu, L. Gu, Z. Hu, X. Wang, Z. Wang, L. Chen, Stacking faults hinder lithium insertion in Li_2RuO_3, Adv. Energy Mater. 10 (2020) 2002631.

[119] M.M. Rahman, J.-Z. Wang, M.F. Hassan, D. Wexler, H.K. Liu, Amorphous carbon coated high grain boundary density dual phase $Li_4Ti_5O_{12}$-TiO_2: A nanocomposite anode material for Li-ion batteries, Adv. Energy Mater. 1 (2011) 212-220.

[120] R.G. Mariano, M. Kang, O.J. Wahab, I.J. McPherson, J.A. Rabinowitz, P.R. Unwin, M.W. Kanan, Microstructural origin of locally enhanced CO_2 electroreduction activity on gold, Nat. Mater. 20 (2021) 1000-1006.

[121] J. Sun, C. Sheng, X. Cao, P. Wang, P. He, H. Yang, Z. Chang, X. Yue, H. Zhou, Restraining oxygen release and suppressing structure distortion in single-crystal Li-rich layered cathode materials, Adv. Funct. Mater. 32 (2021) 2110295.

[122] C. Ma, K. Chen, C. Liang, C.-W. Nan, R. Ishikawa, K. More, M. Chi, Atomic-scale origin of the large grain-boundary resistance in perovskite Li-ion-conducting solid electrolytes, Energy Environ. Sci. 7 (2014) 1638-1642.

[123] A.R. Symington, M. Molinari, J.A. Dawson, J.M. Statham, J. Purton, P. Canepa, S.C. Parker, Elucidating the nature of grain boundary resistance in lithium lanthanum titanate, J.

Mater. Chem. A 9 (2021) 6487-6498.

[124] F.M. Pesci, A. Bertei, R.H. Brugge, S.P. Emge, A.O. Hekselman, L.E. Marbella, C.P. Grey, A. Aguadero, Establishing ultralow activation energies for lithium transport in garnet electrolytes, ACS Appl. Mater. Interfaces 12 (2020) 32806-32816.

[125] T. Thompson, A. Sharafi, M.D. Johannes, A. Huq, J.L. Allen, J. Wolfenstine, J. Sakamoto, A tale of two sites: on defining the carrier concentration in garnet-based ionic conductors for advanced Li batteries, Adv. Energy Mater. 5 (2015) 1500096.

[126] F. Han, A.S. Westover, J. Yue, X. Fan, F. Wang, M. Chi, D.N. Leonard, N.J. Dudney, H. Wang, C. Wang, High electronic conductivity as the origin of lithium dendrite formation within solid electrolytes, Nat. Energy 4 (2019) 187-196.

[127] D. Cao, X. Sun, Q. Li, A. Natan, P. Xiang, H. Zhu, Lithium dendrite in all-solid-state batteries: growth mechanisms, suppression strategies, and characterizations, Matter 3 (2020) 57-94.

[128] C.-L. Tsai, V. Roddatis, C.V. Chandran, Q. Ma, S. Uhlenbruck, M. Bram, P. Heitjans, O. Guillon, $Li_7La_3Zr_2O_{12}$ interface modification for Li dendrite prevention, ACS Appl. Mater. Interfaces 8 (2016) 10617-10626.

[129] H.-K. Tian, Z. Liu, Y. Ji, L.-Q. Chen, Y. Qi, Interfacial electronic properties dictate Li dendrite growth in solid electrolytes, Chem. Mater. 31 (2019) 7351-7359.

[130] Y. Song, L. Yang, W. Zhao, Z. Wang, Y. Zhao, Z. Wang, Q. Zhao, H. Liu, F. Pan, Revealing the short-circuiting mechanism of garnet-based solid-state electrolyte, Adv. Energy Mater. 9 (2019) 1900671.

[131] S. Yu, D.J. Siegel, Grain boundary contributions to Li-ion transport in the solid electrolyte $Li_7La_3Zr_2O_{12}$ (LLZO), Chem. Mater. 29 (2017) 9639-9647.

[132] N. Bernstein, M. Johannes, K. Hoang, Origin of the structural phase transition in $Li_7La_3Zr_2O_{12}$, Phy. Rev. Lett. 109 (2012) 205702.

[133] R. Jalem, Y. Yamamoto, H. Shiiba, M. Nakayama, H. Munakata, T. Kasuga, K.

Kanamura, Concerted migration mechanism in the Li ion dynamics of garnet-type Li$_7$La$_3$Zr$_2$O$_{12}$, Chem. Mater. 25 (2013) 425-430.

[134] T. Thompson, S. Yu, L. Williams, R.D. Schmidt, R. Garcia-Mendez, J. Wolfenstine, J.L. Allen, E. Kioupakis, D.J. Siegel, J. Sakamoto, Electrochemical window of the Li-ion solid electrolyte Li$_7$La$_3$Zr$_2$O$_{12}$, ACS Energy Lett. 2 (2017) 462-468.

[135] A.G. Squires, D.O. Scanlon, B.J. Morgan, Native defects and their doping response in the lithium solid electrolyte Li$_7$La$_3$Zr$_2$O$_{12}$, Chem. Mater. 32 (2019) 1876-1886.

[136] B. Gao, R. Jalem, Y. Tateyama, Surface-dependent stability of the interface between garnet Li$_7$La$_3$Zr$_2$O$_{12}$ and the Li metal in the all-solid-state battery from first-principles calculations, ACS Appl. Mater. Interfaces 12 (2020) 16350-16358.

[137] F. Banhart, J. Kotakoski, A.V. Krasheninnikov, Structural defects in graphene, ACS Nano 5 (2011) 26-41.

[138] A. Krasheninnikov, P. Lehtinen, A. Foster, R. Nieminen, Bending the rules: Contrasting vacancy energetics and migration in graphite and carbon nanotubes, Chem. Phy. Lett. 418 (2006) 132-136.

[139] A. El-Barbary, R. Telling, C. Ewels, M. Heggie, P. Briddon, Structure and energetics of the vacancy in graphite, Phy. Rev. B 68 (2003) 144107.

[140] Z. Shi, Y. Ding, Q. Zhang, J. Sun, Electrocatalyst modulation toward bidirectional sulfur redox in Li-S batteries: From strategic probing to mechanistic understanding, Adv. Energy Mater. 12 (2022) 2201056.

[141] J. Zhu, S. Mu, Defect engineering in carbon‐based electrocatalysts: insight into intrinsic carbon defects, Adv. Funct. Mater. 30 (2020) 2001097.

[142] C. Tang, H.F. Wang, X. Chen, B.Q. Li, T.Z. Hou, B. Zhang, Q. Zhang, M.M. Titirici, F. Wei, Topological defects in metal-free nanocarbon for oxygen electrocatalysis, Adv. Mater. 28 (2016) 6845-6851.

[143] B. Wang, X. Wang, L. Lu, C. Zhou, Z. Xin, J. Wang, X.-k. Ke, G. Sheng, S. Yan, Z. Zou,

Oxygen-vacancy-activated CO_2 splitting over amorphous oxide semiconductor photocatalyst, ACS Catal. 8 (2018) 516-525.

[144] Y.-H. Wang, S. Zheng, W.-M. Yang, R.-Y. Zhou, Q.-F. He, P. Radjenovic, J.-C. Dong, S. Li, J. Zheng, Z.-L. Yang, In situ Raman spectroscopy reveals the structure and dissociation of interfacial water, Nature 600 (2021) 81-85.

[145] K. Ganesan, S. Ghosh, N.G. Krishna, S. Ilango, M. Kamruddin, A. Tyagi, A comparative study on defect estimation using XPS and Raman spectroscopy in few layer nanographitic structures, Phys. Chem. Chem. Phys. 18 (2016) 22160-22167.

[146] H.-Q. Chen, L. Zou, D.-Y. Wei, L.-L. Zheng, Y.-F. Wu, H. Zhang, J.-F. Li, In situ studies of energy-related electrochemical reactions using Raman and X-ray absorption spectroscopy, Chinese J. Catal. 43 (2022) 33-46.

[147] S. Dolabella, A. Borzì, A. Dommann, A. Neels, Lattice strain and defects analysis in nanostructured semiconductor materials and devices by high-resolution X-ray diffraction: Theoretical and practical aspects, Small Methods 6 (2022) 2100932.

[148] H. Hu, Q. Li, L. Li, X. Teng, Z. Feng, Y. Zhang, M. Wu, J. Qiu, Laser irradiation of electrode materials for energy storage and conversion, Matter 3 (2020) 95-126.

[149] L.P. Wang, Y. Leconte, Z. Feng, C. Wei, Y. Zhao, Q. Ma, W. Xu, S. Bourrioux, P. Azais, M. Srinivasan, Novel preparation of N-doped SnO_2 nanoparticles via laser-assisted pyrolysis: Demonstration of exceptional lithium storage properties, Adv. Mater. 29 (2017) 1603286.

[150] Y. Zhang, Z. Ma, D. Liu, S. Dou, J. Ma, M. Zhang, Z. Guo, R. Chen, S. Wang, p-Type SnO thin layers on n-type SnS_2 nanosheets with enriched surface defects and embedded charge transfer for lithium ion batteries, J. Mater. Chem. A 5 (2017) 512-518.

[151] Y. Zheng, T. Zhou, X. Zhao, W.K. Pang, H. Gao, S. Li, Z. Zhou, H. Liu, Z. Guo, Atomic interface engineering and electric-field effect in ultrathin Bi_2MoO_6 nanosheets for superior lithium ion storage, Adv. Mater. 29 (2017) 1700396.

[152] H. Chung, Y. Li, M. Zhang, A. Grenier, C. Mejia, D. Cheng, B. Sayahpour, C. Song,

M.H. Shen, R. Huang, Mitigating anisotropic changes in classical layered oxide materials by controlled twin boundary defects for long cycle life Li-ion batteries, Chem. Mater. 34 (2022) 7302-7312.

[153] H. He, D. Huang, W. Pang, D. Sun, Q. Wang, Y. Tang, X. Ji, Z. Guo, H. Wang, Plasma-induced amorphous shell and deep cation-site S doping endow TiO_2 with extraordinary sodium storage performance, Adv. Mater. 30 (2018) 1801013.

[154] F. Zhang, E. Alhajji, Y. Lei, N. Kurra, H.N. Alshareef, Highly doped 3D graphene Na-ion battery anode by laser scribing polyimide films in nitrogen ambient, Adv. Energy Mater. 8 (2018) 1800353.

[155] W. Yang, J. Zhou, S. Wang, W. Zhang, Z. Wang, F. Lv, K. Wang, Q. Sun, S. Guo, Freestanding film made by necklace-like N-doped hollow carbon with hierarchical pores for high-performance potassium-ion storage, Energy Environ. Sci. 12 (2019) 1605-1612.

[156] H. Lin, L. Yang, X. Jiang, G. Li, T. Zhang, Q. Yao, G.W. Zheng, J.Y. Lee, Electrocatalysis of polysulfide conversion by sulfur-deficient MoS_2 nanoflakes for lithium-sulfur batteries, Energy Environ. Sci. 10 (2017) 1476-1486.

[157] S. Jiang, R. Zhang, H. Liu, Y. Rao, Y. Yu, S. Chen, Q. Yue, Y. Zhang, Y. Kang, Promoting formation of oxygen vacancies in two-dimensional cobalt-doped ceria nanosheets for efficient hydrogen evolution, J. Am. Chem. Soc. 142 (2020) 6461-6466.

[158] Y. Wang, Y. Zhang, Z. Liu, C. Xie, S. Feng, D. Liu, M. Shao, S. Wang, Layered double hydroxide nanosheets with multiple vacancies obtained by dry exfoliation as highly efficient oxygen evolution electrocatalysts, Angew. Chem. Int. Ed. 56 (2017) 5867-5871.

[159] S. Dou, L. Tao, J. Huo, S. Wang, L. Dai, Etched and doped Co_9S_8/graphene hybrid for oxygen electrocatalysis, Energy Environ. Sci. 9 (2016) 1320-1326.

[160] X.R. Wang, J.Y. Liu, Z.W. Liu, W.C. Wang, J. Luo, X.P. Han, X.W. Du, S.Z. Qiao, J. Yang, Identifying the key role of pyridinic-N-Co bonding in synergistic electrocatalysis for reversible ORR/OER, Adv. Mater. 30 (2018) 1800005.

[161] J. Yang, H. Sun, H. Liang, H. Ji, L. Song, C. Gao, H. Xu, A highly efficient metal-free

oxygen reduction electrocatalyst assembled from carbon nanotubes and graphene, Adv. Mater.

28 (2016) 4606-4613.